CNWRA 94-022

NEAR-FIELD LIQUID-VAPOR TRANSPORT IN A PARTIALLY SATURATED HIGH-LEVEL NUCLEAR WASTE REPOSITORY

Prepared for

Nuclear Regulatory Commission
Contract NRC-02-93-005

Prepared by

Center for Nuclear Waste Regulatory Analyses
San Antonio, Texas

October 1994

Rec'd w/ letter dated.
12/30/94

CNWRA 94-022

NEAR-FIELD LIQUID-VAPOR TRANSPORT IN A PARTIALLY SATURATED HIGH-LEVEL NUCLEAR WASTE REPOSITORY

Prepared for

Nuclear Regulatory Commission
Contract NRC-02-93-005

Prepared by

Peter C. Lichtner (CNWRA)
John C. Walton (UT, El Paso)

Center for Nuclear Waste Regulatory Analyses
San Antonio, Texas

October 1994

426.1

ABSTRACT

A fundamental problem in understanding the redistribution of moisture in a high-level nuclear waste repository emplaced in an unsaturated porous host rock is transport of liquid water and water vapor in the near field of the repository. To investigate the assumptions and approximations used in various two-phase flow models of a high-level waste repository, a detailed study was conducted using a repository-scale model. Calculations are presented using CTOUGH, a modified version of the VTOUGH code, for one- and two-dimensional simulations with a cylindrically symmetric repository. The model calculations are based on a disk-shaped heat source providing an average representation of the heat-generating high-level radioactive waste. Both a single homogeneous medium and layer media are considered. The effects of different repository loadings, vapor pressure lowering, and enhanced vapor diffusion on repository dry-out are investigated, as well as formation of heat pipes in the high thermal loading case. Relative humidity is found to be a more sensitive measure of moisture content compared to saturation. It is concluded that the formulation of enhanced vapor diffusion given by Pruess and Tsang (1993, 1994) extrapolated from soil data may grossly overestimate vapor diffusion rates in tuffaceous rock.

CONTENTS

FIGURES

FIGURES (Cont'd)

FIGURES (Cont'd)

TABLES

ACKNOWLEDGMENTS

This report was prepared to document work performed by the Center for Nuclear Waste Regulatory Analyses (CNWRA) for the Nuclear Regulatory Commission (NRC) under Contract No. NRC-02-93-005. The activities reported here were performed on behalf of the NRC Office of Nuclear Material Safety and Safeguards, Division of Waste Management. The report is an independent product of the CNWRA and does not necessarily reflect the views or regulatory position of the NRC.

P. Lichtner would like to thank Mohan Seth for many fruitful discussions during the course of this work. The authors wish to thank M. Seth, C. Freitas, and B. Sagar for reviewing the report.

QUALITY OF DATA, ANALYSES, AND CODE DEVELOPMENT

DATA: There is no CNWRA-generated original data contained in this report. Sources for other data should be consulted for determining the level of quality for those data.

ANALYSES AND CODE DEVELOPMENT: The CTOUGH code is a modification of the VTOUGH (Nitao, 1989) code developed at Lawrence Livermore Laboratory. The CTOUGH code is in the process of being configured under the CNWRA software configuation control Technical Operating Procedure TOP-018. At the present time, CTOUGH does not meet all requirements of TOP-018.

1 INTRODUCTION

Yucca Mountain (YM) is being investigated as a possible site to construct a high-level nuclear waste (HLW) repository. It is proposed to bury HLW in the unsaturated zone several hundred meters above the water table. The motivation for this location for a HLW repository is the relatively dry conditions caused by the partially saturated host rock. The present average rainfall is less than 10 mm/yr. The ambient liquid saturation of the Topopah Spring (TSw) stratigraphic unit, in which it is proposed to dispose of the waste, is approximately 65 percent. The total porosity of the rock matrix is about 10 percent. This still amounts to a large quantity of liquid water, however. Of major concern is the mobilization of this water by boiling and evaporation/condensation processes as a consequence of the large quantity of heat generated by the waste. Following emplacement of the heat-generating waste, complex multiphase mass and heat flow processes are expected to take place. These processes include flow of liquid water, water vapor, and air under pressure gradients; binary diffusion of air and water vapor; conductive and convective heat transfer, phase changes between liquid and gaseous states; capillary and adsorption forces; and gravity (Pruess et al., 1990a,b; Buscheck and Nitao, 1992; Pruess and Tsang, 1993, 1994; Green et al., 1992). Capillary forces give rise to vapor pressure lowering effects causing the boiling point of water to be raised substantially above its nominal value at ambient pressure. To further complicate the situation, these processes take place in a highly fractured, heterogeneous porous medium composed of different stratigraphic units with spatially varying material properties.

1.1 REGULATORY BACKGROUND

The Nuclear Regulatory Commission (NRC) is developing methodologies and techniques for use in determining compliance with its regulation [i.e., 10 CFR Part 60 (Nuclear Regulatory Commission, 1994)] for disposal of HLW in a geologic repository. Computer models and techniques for evaluating compliance with the performance objectives for the overall repository system (i.e., total-system) are being developed under the NRC Iterative Performance Assessment (IPA) program. At this point, these computer models and techniques have been applied in two IPA exercises (Codell et al., 1992; Wescott et al., 1994) for the proposed repository at the YM site in Nevada. Results of the most recent NRC total-system performance assessment (TSPA) for YM, like those of the U.S. Department of Energy (DOE) (Barnard et al., 1992; Wilson et al., 1994), support the general conclusion that the most significant factors controlling the performance of the repository are:

- Percolation flux (and associated fracture-matrix flow)
- Container lifetime (as determined by corrosion processes)
- Water flow past the failed containers

The latter two factors are largely dependent upon the thermohydrologic conditions in the vicinity of the repository. To exploit this dependence, the DOE has proposed a thermal loading strategy referred to as the "extended-dry" concept. In this thermal loading strategy, the radiogenic heat from the waste packages produces a dry-out zone around the repository which persists for an extended period, possibly several thousand years (Buschek and Nitao, 1992). Whether the thermohydrologic conditions produced by the extended-dry concept are beneficial or detrimental to total-system performance is uncertain at this time.

Because of the complex nature of the multiphase mass and heat flow processes associated with the extended-dry concept, it is not possible to realistically account for them in a TSPA model. However, an analysis of this phenomena is possible through the use of sophisticated thermohydrologic computer codes such as VTOUGH (Nitao, 1989), TOUGH2 (Pruess, 1991), or FEHMN (Zysolosky et al., 1992). Although computationally intensive, computer simulations generated by such codes can provide insight to the mobilization of water as a function of (i) fluid pressures (water, vapor, and air); (ii) phase changes between liquid and gaseous states; (iii) capillary, adsorption, and gravity forces; and (iv) binary diffusion of air and water vapor. In addition, thermohydrologic codes can capture interdependencies such as capillary forces giving rise to vapor pressure lowering, which results in the boiling point of water being raised.

An auxiliary analysis was undertaken to develop a quantitative understanding of the thermohydrological phenomena in the near-field region of the repository. Although not precisely defined, the near-field region refers to the thermally perturbed zone. For the proposed repository at YM, the near-field region would extend to the land surface and some distance below the water table, and laterally well beyond the location of the emplaced waste containers. The analysis was performed using the CTOUGH code, which is the CNWRA version of the VTOUGH code.

1.2 OBJECTIVES AND SCOPE

The central objectives of the IPA auxiliary analysis are three-fold: (i) evaluate the theoretical models reviewed in a companion document (Lichtner, 1994), (ii) examine the efficacy of alternate spatial approximations of the near-field region, and (iii) estimate the thermohydrologic conditions for alternate heat loads with emphasis on liquid and vapor fluxes through the repository.

This report focuses on a vertical section through the center of the repository making use of a repository-scale model. This model is based on a disk-shaped repository with cylindrical symmetry. The radius of the disk is related to the areal power density (APD) used in the repository design. Edge effects due to the finite size of the repository are not considered in this report. Both one- (1D) and two-dimensional (2D) calculations are carried out. It is demonstrated that a 1D calculation based on a vertical section through the center of the repository disk gives an almost identical description of the heat and moisture redistribution in the porous rock column compared to a 2D calculation. Only close to the edges of the repository is it expected that large differences could occur. The repository-scale model, however, accounts neither for the finite size of the waste packages nor their finite spacing within the repository, nor does it provide for a detailed representation of fluid transport in the immediate vicinity of a waste package. A companion report analyzes the behavior of the system in the vicinity of a single waste package (Walton and Lichtner, in progress).

1.3 REPORT ORGANIZATION

First, the repository-scale model is introduced, and mass and energy conservation equations solved by the code CTOUGH are reviewed along with constitutive relations for various material properties. The enhanced binary diffusion model proposed by Pruess and Tsang (1993, 1994) is analyzed. The repository is modeled as a disk with gravity pointing vertically downward, enabling cylindrical symmetry to be invoked. Calculations are based on the equivalent continuum model in which a fractured porous medium is represented as a single continuum based on properties of the fracture network and rock matrix. The form of average field properties for the equivalent continuum model are derived. Section 3 begins with the single-layer representation of the repository-scale model. Calculations are performed for

heat loads of 57- and 114-kW/acre APD. A heat-pipe is formed in the high-thermal loading case (114-kW/acre). Vapor transport is found to be downward across the repository horizon, contrary to what is expected from buoyancy effects consistent with Tsang and Pruess (1987). Finally, a multiple-layer model is presented consisting of four different stratigraphic units, and the effect of enhanced vapor diffusion (Pruess and Tsang, 1993, 1994) is investigated. Enhanced binary diffusion is shown to have a pronounced effect at low heat loads but only a minor impact at the 114-kW/acre APD heat load.

2 REPOSITORY-SCALE MODEL

The near-field region of a HLW repository, defined in this and the following sections as the region extending vertically from the ground surface to the water table, can be expected to undergo substantial changes from ambient conditions. These changes are caused by heat generated from the waste products as they decay with time.

For computational reasons, it is useful to simplify the geometry of the repository. The repository emplacement is assumed to be horizontal with gravity acting vertically downward. A simplified model is used in which the repository is represented by a disk of zero thickness as shown in Figure 2-1. The radius of the disk is adjusted to give the appropriate initial APD.

First, a simplified 1D model is considered in order to obtain a rough idea of the changes in temperature, pressure, and saturation state in the near-field region of the repository. The host rock is assumed to be homogeneous throughout in order to simplify the calculations. Next, a multilayer model is used to account for the various stratigraphic units at YM.

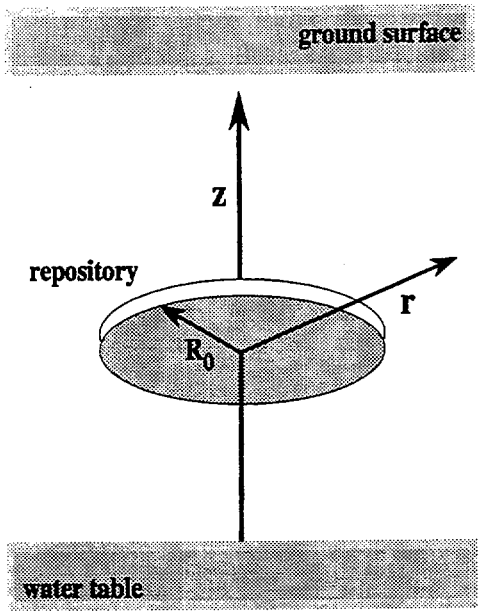

Figure 2-1. Schematic diagram of the cylindrically symmetric repository-scale model

2.1 MODEL DESCRIPTION

The redistribution of heat and mass can be described by a set of partial differential equations representing conservation laws combined with algebraic constraints for gas-liquid equilibria. Two chemical reactions are allowed to take place. The first is boiling, evaporation, and condensation of water described by the reaction

$$H_2O_{(l)} \Leftrightarrow H_2O_{(g)}, \tag{2-1}$$

with reaction rate I_{H_2O}. The rate is assumed to be positive for evaporation and negative for condensation. The second is partitioning of air (here considered as a single component) between gas and liquid phases

$$Air_{(l)} \Leftrightarrow Air_{(g)}, \tag{2-2}$$

with reaction rate I_{Air}. Many other reactions can also take place that could influence the near-field response of the system to the heat generated by the repository. These include homogeneous reactions within the aqueous and gas phases, and mineral precipitation and dissolution reactions resulting from dilution and concentration of solute species by liquid evaporation and condensation, as well as reaction with the primary host mineral assemblage. These reactions, however, while potentially important, are reserved for a later report.

2.1.1 Mass Conservation

Mass conservation equations for the two-component (water, air), two-phase (liquid, gas) system are given for water by the equations

$$\frac{\partial}{\partial t}(\varphi \rho_l s_l w_w^l) + \nabla \cdot F_w^l = -I_{H_2O}, \tag{2-3}$$

and

$$\frac{\partial}{\partial t}(\varphi \rho_g s_g w_w^g) + \nabla \cdot F_w^g = I_{H_2O}, \tag{2-4}$$

and for air by the equations

$$\frac{\partial}{\partial t}(\varphi \rho_l s_l w_a^l) + \nabla \cdot F_a^l = -I_{Air}, \tag{2-5}$$

and

$$\frac{\partial}{\partial t}(\varphi \rho_g s_g w_a^g) + \nabla \cdot F_a^g = I_{Air}, \tag{2-6}$$

where φ denotes the porosity, $\rho_{l,g}$ denotes the density, $s_{l,g}$ denotes the saturation, $w_w^{l,g}$ denotes the mass fraction of water, and $F_w^{l,g}$ refers to the flux of water in the liquid and gas phases. The liquid and gas fluxes for water are given, respectively, by

$$F_w^l = w_w^l q_l, \tag{2-7}$$

and

$$F_w^g = w_w^g q_g + q_w^D, \tag{2-8}$$

where $q_{l,g}$ denotes the liquid and gas Darcy velocities, and q_w^D denotes the diffusive flux in the gas phase. The diffusive flux of water vapor and air in the liquid phase is negligible and, therefore, is ignored. The liquid and gas fluxes for air are given, respectively, by

$$F_a^l = w_a^l q_l, \tag{2-9}$$

and

$$F_a^g = w_a^g q_g + q_a^D. \tag{2-10}$$

The Darcy velocities for the liquid and gas phases are given by

$$q_l = -\frac{kk_l^r}{\mu_l}(\nabla P_l - \rho_l g), \tag{2-11}$$

and

$$q_g = -\frac{kk_g^r}{\mu_g}(\nabla P_g - \rho_g g), \tag{2-12}$$

where k denotes the permeability, $k_{l,g}^r$ denotes the relative permeability of the liquid and gas phases, and g denotes the acceleration of gravity. Liquid and gas pressures are related by the capillary pressure P_c

$$P_g = P_l + P_c, \tag{2-13}$$

and the total gas pressure is the sum of vapor P_v and air P_a partial pressures:

$$P_g = P_v + P_a. \tag{2-14}$$

The diffusive flux of water vapor is assumed to obey Fick's law

$$q_w^D = -\tau\varphi s_g \rho_g D \nabla w_w^g, \tag{2-15}$$

where τ denotes the tortuosity, and D denotes the binary diffusion coefficient for water vapor and air,

related to temperature and pressure by the expression (Vargaftik, 1975; Walker et al., 1981)

$$D = \frac{D_0 [(T + 273.15)/273.15]^{\theta}}{P/P_0}, \tag{2-16}$$

where D_0 is the binary diffusion coefficient at standard conditions P_0 = 1 bar, T_0 = 273.15 °C, and θ is a constant. The diffusive flux of air in the gas phase is given by

$$q_a^D = -\tau\phi s_g \rho_g D \nabla w_a^g. \tag{2-17}$$

The phase densities are determined as a mixture of pure phases according to the expression

$$\rho_\pi = \sum_{i = w, a} f_i^\pi w_i^\pi \rho_i^\circ, \tag{2-18}$$

where ρ_i° represents the pure phase density of the subscripted species, and the sum is over the components water and air, for π = liquid and gas phases. The weighting factor f_i^π is defined by

$$f_i^\pi = \frac{1}{M_i \sum_l w_l^\pi (M_l)^{-1}}, \tag{2-19}$$

where M_i denotes the formula weight of the ith species.

The four mass conservation equations can be reduced to two equations under conditions of local chemical equilibrium by combining the differential equations with algebraic equations expressing equilibrium of the above reactions. The reaction rate for evaporation and condensation of water can be eliminated from the mass conservation equations by adding the liquid and gas phase conservation equations to yield a single partial differential equation for the conservation of water given by

$$\frac{\partial}{\partial t}[\varphi (\rho_l s_l w_w^l + \rho_g s_g w_w^g)] + \nabla \cdot (F_w^l + F_w^g) = 0. \tag{2-20}$$

This equation is useful for conditions of local equilibrium in which the reaction rate is determined by transport and is not known until after the mass and energy conservation equations have been solved. The evaporation rate can be calculated by differentiation using Eqs. (2-3) or (2-4) once the conservation equations have been solved. Although both equations must give identical results, because Eq. (2-3) does not involve the diffusive flux it is preferred. A similar equation exists for air obtained by adding Eqs. (2-5) and (2-6) to give

$$\frac{\partial}{\partial t}[\varphi (\rho_l s_l w_a^l + \rho_g s_g w_a^g)] + \nabla \cdot (F_a^l + F_a^g) = 0, \tag{2-21}$$

in which the rate of reaction for partitioning air between liquid and gas phases is eliminated.

2.1.2 Energy Conservation

The energy conservation equation is given by

$$\frac{\partial}{\partial t}[\varphi(\rho_l s_l u_l + \rho_g s_g u_g) + (1-\varphi)\rho_{\text{rock}} C_P T] + \nabla \cdot \left(h_l q_l + h_g q_g\right) - \nabla \cdot K \nabla T = Q(t), \qquad (2\text{-}22)$$

where ρ_{rock} denotes the density of the host rock, K denotes the thermal conductivity, $Q(t)$ denotes the volumetric heat source, and the internal energy $u_{l,g}$ and enthalpy $h_{l,g}$ are given in terms of pure phases by the expressions

$$u_\pi = \sum_{i=w,a} f_i^\pi w_i^\pi u_i^\circ, \qquad (2\text{-}23)$$

and

$$h_\pi = \sum_{i=w,a} f_i^\pi w_i^\pi h_i^\circ. \qquad (2\text{-}24)$$

The thermal conductivity is averaged over the solid and fluid phases.

Equations (2-20), (2-21), and (2-22) are solved simultaneously by CTOUGH with specified initial and boundary conditions, and appropriate thermodynamic constraints depending on the number of phases present at a given point in the system. The equivalent continuum model with van Genuchten constitutive relations for material properties of capillary suction as a function of saturation and relative permeability is employed.

2.1.3 Heat Load

The APD is defined as the initial power produced by the heat-generating waste per unit area:

$$\text{APD} = \frac{M_0 \Gamma_0}{A}, \qquad (2\text{-}25)$$

where A denotes the average area of the repository, M_0 represents the total inventory of heavy metal contained in the repository in metric tons, and Γ_0 represents the heat generation rate in watts per metric ton initial heavy metal (MTIHM). The input to CTOUGH is the heat generation rate $\wp(t)$ in units of watts defined in terms of the APD by

$$\wp(t) = M_0 \Gamma(t) = A \times \text{APD} \frac{\Gamma(t)}{\Gamma_0}. \qquad (2\text{-}26)$$

The normalized heat generation rate $\Gamma(t)/\Gamma_0$ is calculated using a *Mathematica* (Wolfram, 1991) program to generate input data for the CTOUGH code. The values calculated are shown in Figure 2-2. The radius of the repository R_0 is given by

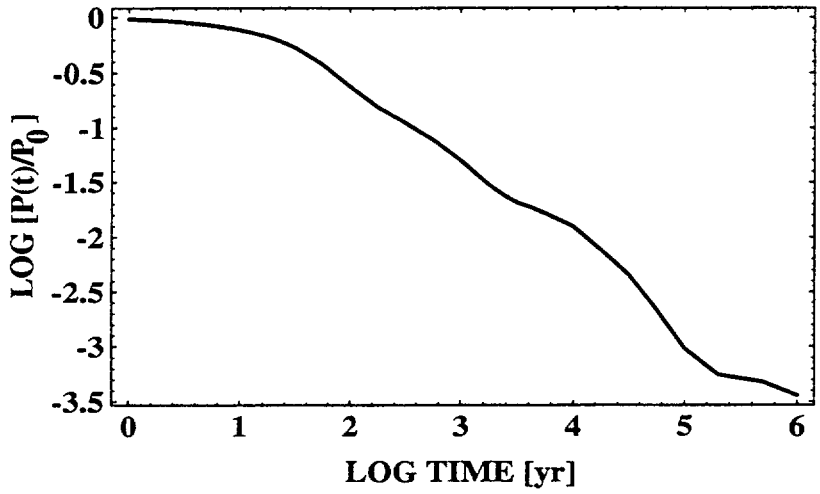

Figure 2-2. The normalized decay heat produced by 10-yr-old spent fuel

$$R_0 = \sqrt{\frac{M_0 \Gamma_0}{\pi \mathrm{APD}}}. \tag{2-27}$$

Thus, for a given mass of HLW, the radius of the repository is inversely proportional to the square root of the APD.

2.2 MATERIAL PROPERTY CONSTITUTIVE RELATIONS

2.2.1 van Genuchten Relations

Constitutive relations for saturation and relative permeability used in the model calculations are taken as the van Genuchten equations (van Genuchten, 1980). These relations define capillary pressure and relative permeability as functions of liquid saturation. The liquid saturation is defined by the expression:

$$s_{\mathrm{eff}} = \frac{1}{[1 + (\alpha |P_c|)^m]^\lambda}, \tag{2-28}$$

where s_{eff} denotes the effective saturation defined by

$$s_{\mathrm{eff}} = \frac{s_l - s_r}{1 - s_r}, \tag{2-29}$$

where s_l denotes the liquid saturation and s_r the residual saturation, P_c represents the capillary pressure,

and α, m, and λ are fit parameters, in general, a function of various rock properties and temperature, with

$$\lambda = 1 - \frac{1}{m}. \tag{2-30}$$

Alternatively, the capillary pressure can be expressed as a function of the effective saturation according to the inverse relation

$$P_c = \frac{1}{\alpha}\left[s_{\text{eff}}^{-1/\lambda} - 1\right]^{\frac{1}{m}}. \tag{2-31}$$

The relative permeability is given by the equation

$$k_l^r = \sqrt{s_{\text{eff}}}\left[1 - \left(1 - s_{\text{eff}}^{-1/\lambda}\right)^{\lambda}\right]^2, \tag{2-32}$$

with the assumption

$$k_l^r + k_g^r = 1. \tag{2-33}$$

For very small capillary pressure approaching zero, the saturation and relative permeability tend to unity. As the capillary pressure becomes increasingly negative, the effective saturation tends toward zero, and the liquid saturation approaches the residual saturation. The relative permeability becomes zero in this limit.

2.2.2 Vapor Pressure Lowering

A crucial effect in determining the boiling point of water in a partially saturated porous medium is the lowering of the vapor pressure of water due to the presence of capillary forces. The vapor pressure P_v is given in terms of the saturation pressure; P_{sat} by the Kelvin equation

$$P_v = P_{\text{sat}}(T)\, e^{-P_c M_w / \rho_l RT}, \tag{2-34}$$

where P_c denotes the capillary pressure, M_w denotes the formula weight of water, and ρ_l represents the density of pure water, a function of temperature and pressure. The exponential factor is the relative humidity h in the presence of liquid and gas phases:

$$h(T) = \frac{P_v}{P_{\text{sat}}(T)} = e^{-P_c M_w / \rho_l RT}. \tag{2-35}$$

The boiling point of water T_b is determined directly from this equation by equating the vapor pressure to the ambient pressure P_0 of the system and solving for T_b:

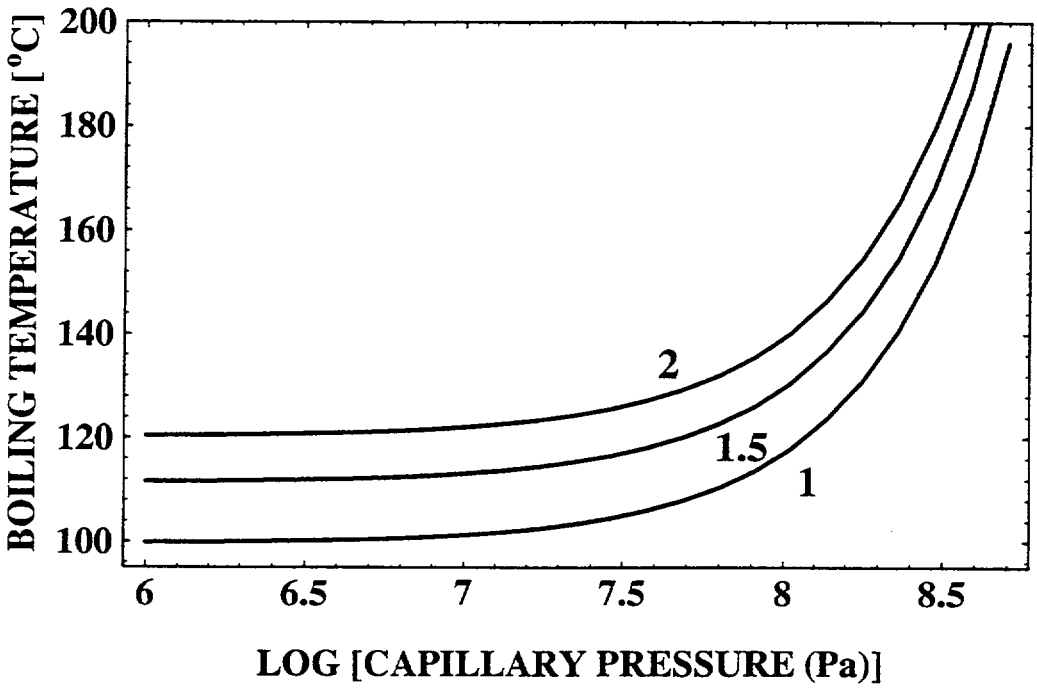

Figure 2-3. The boiling point of water plotted as a function of the logarithm of the capillary pressure for different ambient pressures of 1, 1.5, and 2 bars (see text for parameters used)

$$P_v(T_b) = P_{sat}(T_b)\, e^{-P_c M_w / \rho_l(T_b, P_0) R T_b} = P_0 . \tag{2-36}$$

This provides an expression for the boiling point in terms of the capillary pressure, which can also be expressed in terms of the saturation using the appropriate material property constitutive relation such as Eq. (2-28), based on the van Genuchten relation.

The effect of vapor pressure lowering on the boiling point of water is illustrated in Figure 2-3. The boiling temperature T_b for ambient pressures of 1, 1.5, and 2 bars is plotted as a function of the logarithm of the capillary pressure from Eq. (2-36) with the capillary pressure calculated from the van Genuchten constitutive relation Eq. (2-31). The curves are plotted using matrix properties for YM tuff given in Table 3-1. This figure shows how the boiling point of pure water as calculated in the code CTOUGH varies with capillary pressure. As can be seen from Figure 2-3, the boiling point rises sharply as the capillary pressure increases. The very large values of capillary pressure must be interpreted as adsorption of water rather than pore size effects (Pruess et al., 1990a). Using Eq. (2-31), giving the relationship between capillary pressure and saturation, the boiling point can be plotted as a function of saturation as shown in Figure 2-4. The high capillary suction corresponds to extremely dry conditions. For a capillary tube of radius R_0, the thickness δ of a thin film of water is related to the liquid saturation by the expression

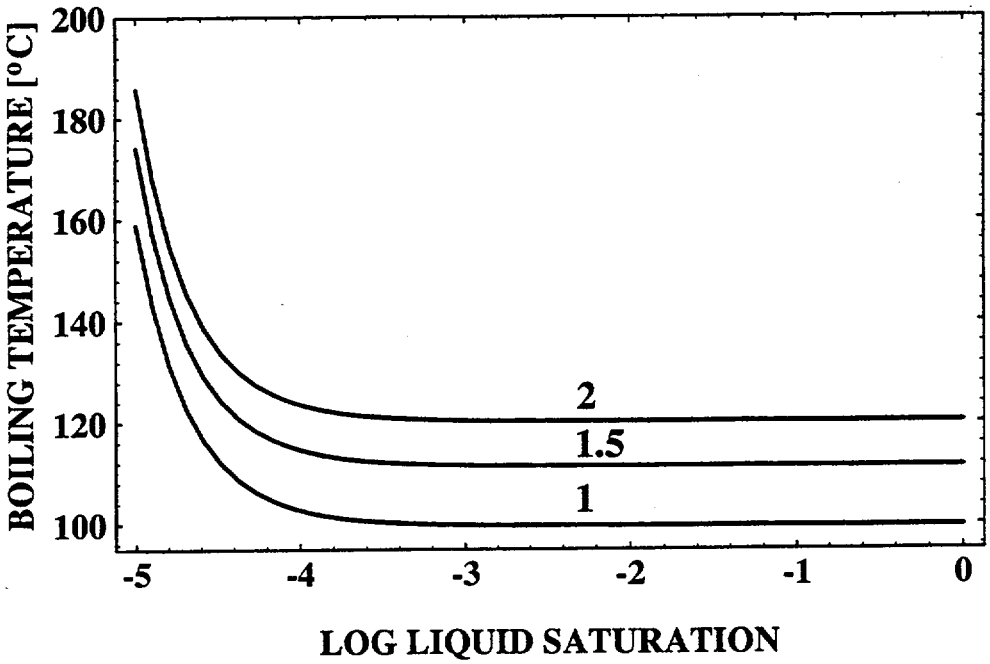

Figure 2-4. The boiling point of water plotted as a function of the logarithm of liquid saturation for different ambient pressures of 1, 1.5, and 2 bars (see text for parameters used)

$$\delta = \frac{1}{2} s_l R_0, \tag{2-37}$$

valid for $\delta \ll R_0$. For a tube of radius 2 mm and liquid saturation 10^{-5}, $\delta = 0.1 \mu m$.

The sensitivity of the boiling point on the van Genuchten parameters α and m is shown in Figures 2-5 and 2-6, respectively. As the saturation is reduced, the boiling temperature changes dramatically with slight changes in the parameters α and m.

2.2.3 Enhanced Vapor Diffusion

Laboratory experiments measuring the transport of water vapor in soils under the influence of a temperature gradient suggest that transport is greatly enhanced compared to what would be predicted by Fick's law (Jury and Letey, 1979). Enhancement is believed to result from the presence of islands of liquid water in the partially saturated pore spaces. In the work of Pruess and Tsang (1993, 1994), enhanced vapor transport is introduced by replacing the quantity β, given as the product of tortuosity, porosity, and gas saturation [see Eq. (2-15)] with unity: $\beta = \tau \varphi s_g \rightarrow 1$. In this case, the diffusive flux for water vapor has the form

$$q_w^D = -\beta \rho_g D \nabla w_w^g. \tag{2-38}$$

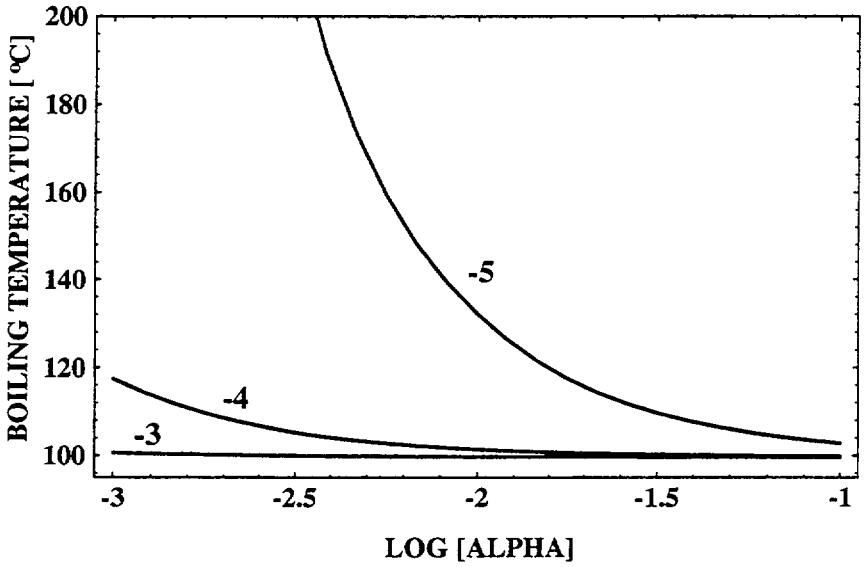

Figure 2-5. The boiling point of water plotted as a function of the logarithm of the van Genuchten parameter α for different liquid saturations of log s_l = –3, –4, –5 (see text for parameters used)

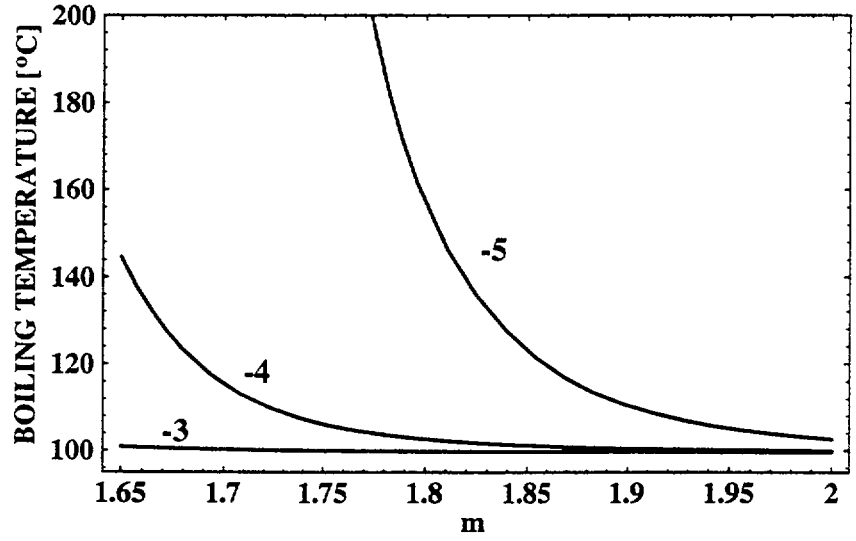

Figure 2-6. The boiling point of water plotted as a function of the van Genuchten parameter m for different liquid saturations of log s_l = –3, –4, –5 (see text for parameters used)

Pruess and Tsang (1993, 1994) justify this assumption based on experimental observations of vapor transport in soils. Jury and Letey (1979) review literature values for β, which range from 0.9 to 3.8 and derive an average value of 1.8. However, it must be pointed out that their results may be restricted to clay-like materials and sandy soils and may not apply to the tuffaceous rock found at YM. Furthermore, the temperature range of available data is limited to relatively low temperatures. The value for β tends to decrease for liquid saturation above about 70 percent, and decreases with increasing temperature. In any event, the results obtained from model calculations are rather sensitive to the value chosen for β for low heat loads, as illustrated in Sections 3.1.3 and 3.2.2.

From a theoretical point of view, there seems to be little justification in extrapolating from soils to the tuffaceous rock at YM and assuming the same factor β would apply to both (see Section 2.3.6). Both the rock porosity, which ensures that the mass conservation equations balance fluid transport only in the porous portion of the bulk rock mass and not in the solid part, and the tortuosity would be expected to result in different values for β. The formulation of Pruess and Tsang (1993, 1994) would imply that the vapor flux is the same as soils, even for stratigraphic units with different values for the product of porosity times tortuosity, which seems unreasonable.

An alternative form for the diffusion rate of water vapor which eliminates these deficiencies can be described as:

$$N_{H_2O} = -\frac{\omega\tau\varphi sD}{RT}\nabla P = -sD_{\text{eff}}\frac{\nabla P}{RT}, \tag{2-39}$$

where ω, an acceleration factor for water vapor diffusion relative to diffusion of other gases is introduced, and the other variables are as previously defined (Bird et al., 1960). The effective diffusion coefficient is defined as

$$D_{\text{eff}} = \omega\tau\varphi D = \beta D, \tag{2-40}$$

where β represents an enhancement factor for binary diffusion which is different for different porous media. An estimate of the acceleration and enhancement factors is presented in Section 2.3.6.

2.3 EQUIVALENT CONTINUUM MODEL

2.3.1 Concept of the Equivalent Continuum Model

The main idea behind the equivalent continuum model is to represent a fractured rock mass made up of a matrix characterized by one set of values for porosity and permeability and a fracture network characterized by another set as a single continuum with properties of both the matrix and fracture network (Peters and Klavetter, 1988; Pruess et al., 1990b). The equivalent continuum model thus replaces a porous medium composed of two continua corresponding to fractures and matrix by a single continuum with properties that reflect the individual fracture and matrix continua. Thermodynamic equilibrium is assumed between fracture and matrix field variables such as pressure, temperature, capillary pressure, and solute concentration. The equivalent continuum model leads to a great simplification of the problem, both from a computational standpoint and, more importantly, in terms of the physical processes being modeled. Whether the model is able to represent reality with sufficient accuracy is open to question.

2.3.2 Definition of Field Variables

Properties of the equivalent continuum model are derived by considering a representative elemental volume (REV) containing both fractures and the rock matrix. Fundamental to the concept of the equivalent continuum model is the unique definition of pressure, temperature, solute concentration, etc., throughout the equivalent continuum REV. The volume V of the REV is a sum of contributions from the fracture network and matrix

$$V = V_f + V_m \quad , \tag{2-41}$$

where V_f denotes the fracture REV, and V_m denotes the representative matrix REV volume. It should be noted that partitioning the porous medium into fracture and matrix properties need not be unique and is partly a matter of convenience. This is because the boundary separating the fracture and matrix cannot be uniquely defined especially when solid filling is present. The fracture network is assumed to consist of interconnected void volume without the presence of solids. Although this assumption is an over-simplification which neglects fracture filling and roughness, it may be easily removed, if desired. The equivalent continuum model fracture porosity is defined simply as the ratio of fracture void volume divided by the REV of the equivalent continuum model given by the expression

$$\varphi_f = \frac{V_f}{V} . \tag{2-42}$$

The intrinsic matrix porosity is defined by the ratio of the matrix void volume to the matrix REV

$$\varphi_m = \frac{V_m^p}{V_m} , \tag{2-43}$$

where V_m^p denotes the matrix void volume. Note that, as defined here, the fracture porosity refers to the equivalent continuum medium, whereas the matrix porosity is the intrinsic porosity of the rock matrix defined in terms of the matrix REV and not the equivalent continuum REV. This distinction between matrix and equivalent continuum REV is generally negligible if the equivalent continuum fracture porosity is sufficiently small. With these relations, the total porosity of the equivalent continuum medium is given as the ratio of the total pore volume in the equivalent continuum REV divided by the REV volume:

$$\varphi = \frac{V_p}{V} = \frac{V_f + V_m^p}{V} = \frac{V_f}{V} + \frac{V_m^p}{V_m}\frac{V_m}{V} = \varphi_f + (1-\varphi_f)\varphi_m . \tag{2-44}$$

Because generally $\varphi_f \ll \varphi_m$, it follows that $\varphi \cong \varphi_m$.

Other field variables may be defined similarly in terms of their fracture and matrix counterparts. The liquid saturation of the equivalent continuum model is thus given by the ratio of the total liquid volume contained in fractures and matrix to the REV volume

$$s_l = \frac{V_l}{V}. \tag{2-45}$$

This relation can be expressed in terms of the fracture and matrix saturation defined, respectively, by

$$s_f^l = \frac{V_f^l}{V_f}, \tag{2-46}$$

and

$$s_m^l = \frac{V_m^l}{V_m}. \tag{2-47}$$

It then follows that

$$s_l = \frac{V_f^l + V_m^l}{V_f + V_m} = \frac{\varphi_f s_f^l + (1-\varphi_f)\varphi_m s_m^l}{\varphi}. \tag{2-48}$$

The main postulate on which the equivalent continuum model rests is the assumption of thermodynamic equilibrium between the matrix and fracture network. This implies equality of capillary pressure between the fracture and matrix at their respective saturation states

$$P_{\text{cap}}^f(s_f^l) = P_{\text{cap}}^m(s_m^l). \tag{2-49}$$

Equation (2-49) together with the expression for the saturation of the equivalent continuum model given by Eq. (2-48) provide two simultaneous equations to determine the fracture and matrix saturations for a given composite saturation. Thus at each point in space, the equivalent continuum model assigns average saturations for both fracture and matrix as well as the composite value. These relations lead to very stringent conditions on the flow properties in the fracture network, requiring almost fully saturated conditions in the matrix before fluid flow in the fracture can commence. This property of the equivalent continuum model can greatly underestimate fracture flow under transient conditions.

2.3.3 Permeability

An expression for the equivalent continuum permeability and relative permeability can be obtained by equating the volumetric flux in the equivalent continuum medium to the sum of the fluxes in the fracture and matrix:

$$Q = Q_f + Q_m. \tag{2-50}$$

The volumetric flow rate Q is related to the Darcy velocity q by the cross section flow area A according to the expression

$$Q = Aq, \tag{2-51}$$

with the Darcy velocity given by

$$q = -\frac{kk_r}{\mu}\nabla p. \tag{2-52}$$

From Eqs. (2-50) and (2-51) applied to each continuum separately, it follows that

$$q = \frac{A_f q_f + A_m q_m}{A}. \tag{2-53}$$

Assuming that the area and volume porosities are the same

$$\frac{A_f}{A} = \frac{V_f}{V} = \varphi_f, \tag{2-54}$$

and

$$\frac{A_m}{A} = \frac{V_m}{V} = 1 - \varphi_f, \tag{2-55}$$

it follows that

$$kk_r = \varphi_f k_f k_f^r + (1 - \varphi_f) k_m k_m^r. \tag{2-56}$$

Accordingly, the equivalent continuum permeability may be defined as

$$k = \varphi_f k_f + (1 - \varphi_f) k_m, \tag{2-57}$$

and the relative continuum permeability as

$$k_r = \frac{\varphi_f k_f k_f^r + (1 - \varphi_f) k_m k_m^r}{\varphi_f k_f + (1 - \varphi_f) k_m}. \tag{2-58}$$

2.3.4 Diffusive Flux

The diffusive flux of a solute species may be treated similarly. The equivalent continuum flux is related to the fracture and matrix fluxes by the expression

$$AF = A_f F_f + A_m F_m, \tag{2-59}$$

with the diffusive flux F defined as

$$F = -\varphi D \nabla C . \tag{2-60}$$

For the fracture network the diffusive flux is given by

$$F_f = -D_f \nabla C , \tag{2-61}$$

since the fracture is presumed to be devoid of solid and, therefore, has unit intrinsic porosity. The matrix diffusive flux is given by

$$F_m = -\varphi_m D_m \nabla C . \tag{2-62}$$

Combining these relations yields an expression for the equivalent continuum diffusion coefficient given by

$$D = \frac{\varphi_f D_f + (1-\varphi_f)\varphi_m D_m}{\varphi_f + (1-\varphi_f)\varphi_m} . \tag{2-63}$$

The diffusion coefficients which appear in this expression represent effective values which include the effects of tortuosity and gas saturation. Thus, if

$$D = \tau s_g D_0 , \tag{2-64}$$

with similar expressions for fracture and matrix continua, where τ represents the tortuosity, and D_0 refers to the diffusion coefficient in a pure gas or liquid phase, then a relation can be derived between the tortuosities of the equivalent continuum, matrix, and fracture network given by

$$\tau = \frac{\tau_f s_g^f \varphi_f + \tau_m s_g^m (1-\varphi_f)\varphi_m}{\varphi s_g} . \tag{2-65}$$

For the situation in which

$$\tau_f = \tau_m , \tag{2-66}$$

it follows that

$$\tau = \tau_m = \tau_f . \tag{2-67}$$

This relation holds regardless of the values of the gas saturation in the fracture and matrix continua.

2.3.5 Porosity-Permeability Relations for Yucca Mountain Tuff

An empirical relation between porosity and permeability for YM tuff was obtained by fitting porosity-permeability data to a power law relation given by

$$k = k_0\left(\frac{\varphi}{\varphi_0}\right)^n, \tag{2-68}$$

where k denotes the permeability and φ the porosity, and the subscripted quantities k_0, φ_0 refer to an arbitrary point. On a log-log scale this equation implies a linear relationship between the logarithms of the porosity and permeability given by

$$\log\varphi = \frac{1}{n}(\log k - \log k_0) - \log\varphi_0. \tag{2-69}$$

The result using the data listed in Table 2-1, obtained by averaging over each stratigraphic unit, is shown in Figure 2-7 for two values of the power n equal to 7 and 3, corresponding to the upper and lower straight lines, respectively. The curves are constrained arbitrarily to pass through the point labeled 11. The numbers in the figure correspond to the stratigraphic units listed in Table 2-1. The fit is reasonably good considering the wide spread in porosity, permeability, and diversity of rock types. The two outlying points numbered 8 and 19; both refer to vitrified tuff and, thus, could be expected to have different properties from the other samples. Because of the low slope of the $n = 7$ line, porosity values lying between 5 to 10 percent correspond to almost four orders of magnitude change in permeability.

2.3.6 Tortuosity/Effective Diffusion Coefficient

One important area of uncertainty at YM is the diffusion rate of water vapor through tuff rock. Major concerns are: (i) general lack of diffusion data through tuff rock, (ii) influence of fractures and other heterogeneities on diffusion, and (iii) accelerated diffusion of water vapor, a condensable gas, relative to diffusion of other gases. This section examines some of the factors involved and the current understanding of the problem.

An important question is what portion of the media, fractures or matrix, dominates vapor diffusion. For Darcy flow of vapor, the fractures have a much higher permeability than the rock matrix and clearly dominate. For vapor diffusion, the relative roles of matrix and fracture transport are not as clear. The experimental work of Ali et al. (1994) can be used to examine the $\tau\varphi$ factor included in the effective diffusion coefficient. The data are for diffusion of carbon dioxide gas through a dried sample of tuff rock matrix. The gas saturation is taken as one, and the acceleration factor (ω) is assumed to be one (noncondensable gas). Division of the experimentally determined effective diffusion coefficient by the temperature-corrected binary diffusion coefficient for air/carbon dioxide gives an estimate of $\tau\varphi$. The result for several rock samples over a temperature range of 0 to 150 °C is presented in Figure 2-8. If the diffusion process could be described strictly by binary diffusion, the curves should be horizontal straight lines. However, this is not the case, indicating that the experimental data may involve both Knudsen and ordinary diffusion. Analysis of the data assuming Knudsen diffusion dominates can be performed using

$$D^K = \frac{2\varphi r_e}{3}\sqrt{\frac{8RT}{\pi M}}, \tag{2-70}$$

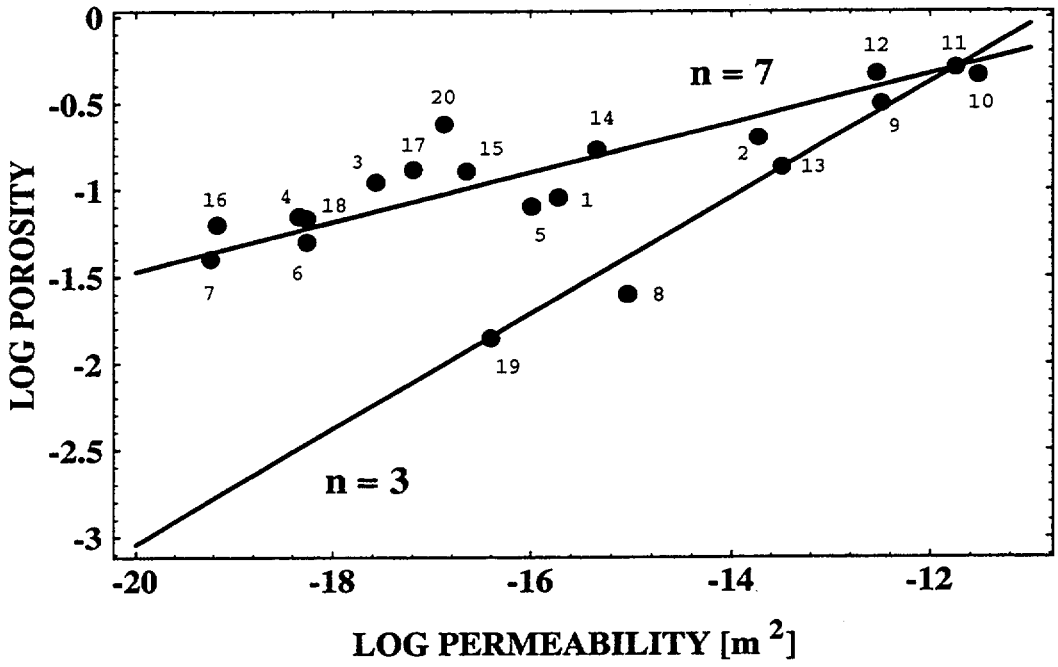

Figure 2-7. Fit to porosity-permeability data from Yucca Mountain tuff

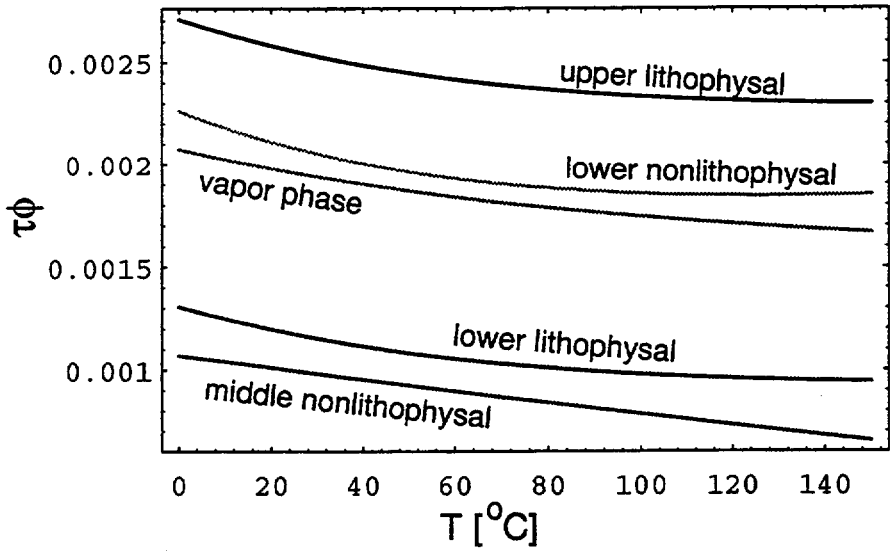

Figure 2-8. Estimated τφ from carbon dioxide diffusion assuming ordinary diffusion

Table 2-1. Porosity-permeability data taken from INTRAVAL Study Phase 2, prepared by Golde Associates, Reference 913-10024.202, April 29, 1992, Attachment A

Member	Point	Unit	Porosity	Permeability m^2
Tiva Canyon	1	Caprock	0.09	1.898e-16
	2	Upper Cliff	0.2	1.860e-14
	3	Upper Lithophysal	0.11	2.715e-18
	4	Clinkstone	0.07	4.607e-19
	5	Lower Lithophysal	0.07	1.027e-16
	6	Hackley	0.05	5.541e-19
	7	Columnar	0.04	5.908e-20
	8	Vitrophyre	0.025	9.224e-16
	9	Shardy Base	0.315	3.249e-13
Nonwelded Bedded Tuffs	10	Yucca Mountain	0.46	3.027e-12
	11	Pahcanyon	0.51	1.795e-12
Topopah Spring	12	Nonwelded	0.47	2.907e-13
	13	Caprock	0.135	3.247e-14
	14	Rounded	0.17	4.580e-16
	15	Upper Lithophysal	0.1275	2.241e-17
	16	Middle Nonlithophysal	0.063	6.903e-20
	17	Lower Lithophysal	0.13	6.459e-18
	18	Lower Nonlithophysal	0.068	5.495e-19
	19	Vitrophyre	0.014	3.950e-17
Calico Hills	20	Calico Zeolite	0.24	1.322e-17

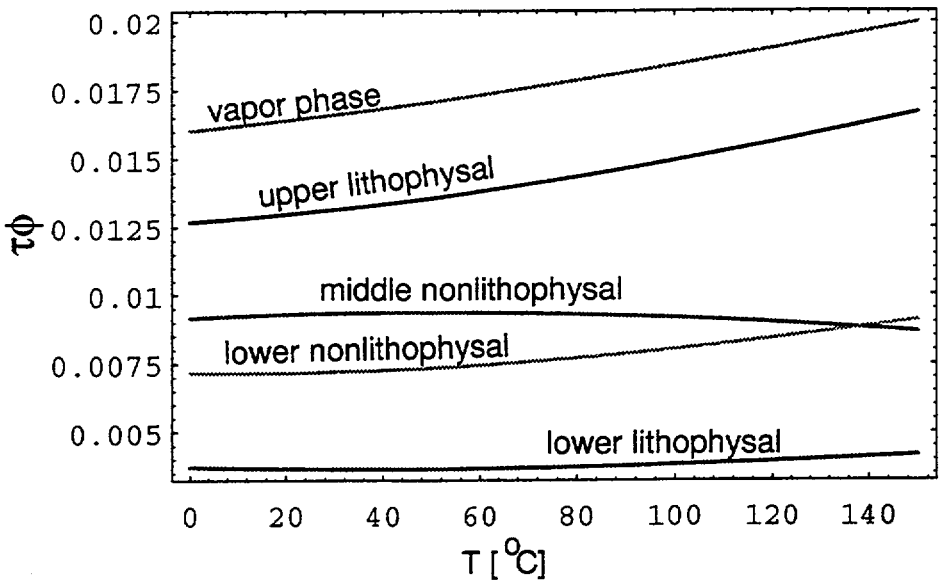

Figure 2-9. Estimated τφ from carbon dioxide diffusion assuming Knudsen diffusion

where r_e is the effective pore radius. To estimate the tortuosity it is assumed that the experimentally reported average pore radius is equivalent to the effective pore radius for Knudsen diffusion. This assumption is unlikely to be accurate. The resulting estimates of τφ for the different rock units are presented in Figure 2-9. The resulting tortuosity differs from that obtained assuming binary diffusion by an order of magnitude. However, this is presumably a consequence of poor knowledge of the Knudsen diffusion coefficient. For Knudsen diffusion, the curves tend to bend upward rather than downward, as in the case of binary diffusion, indicating that the actual diffusion process probably lies in the transition region between binary and Knudsen diffusion. However, note that the curve for the lower lithophysal unit becomes much straighter with Knudsen diffusion compared to binary diffusion.

The acceleration factor ω can be determined from the data in Jury and Letey (1979) who derive an average value of 1.8 for β from the available literature measurements on soils. For an order of magnitude, assume that the soils have a porosity of 0.3 and water vapor diffusion responds to total porosity (not vapor filled porosity). Tortuosity is approximated as $\varphi^{1/3}$. This gives a value of $\omega = 1.8/0.3/0.3^{1/3} = 9$. Next, assuming the same acceleration occurs in desiccated rocks at higher temperatures, an initial estimate of β for tuff rock is:

$$\beta = \omega\tau\varphi \cong 9 \times (0.0001 \text{ to } 0.003) = 0.0009 \text{ to } 0.027\,, \tag{2-71}$$

as estimated from the binary diffusion fit with the range of variables shown in Figure 2-8. Thus, based on limited experimental data and approximate calculations, the estimated diffusion rate is a factor of 35 to 1,000 lower than the value β = 1 used by Pruess and Tsang (1994). Hence, there would appear to be little justification for enhanced vapor diffusion as implemented by Pruess and Tsang (1994).

Another consideration is the role of matrix versus fractures in water vapor transport. Assuming the acceleration factor for soils at low temperatures (~9) is equal to the rock matrix and fracture enhancement factor at higher temperatures, it is possible to estimate the relative role of matrix and fractures in vapor diffusion. If these assumptions are valid, the relative roles of matrix and fracture can be estimated by comparison of the product $\tau\varphi$. Assuming a tortuosity of unity for fractures and a fracture porosity of 0.01 to 0.0001, a product of 10^{-2} to 10^{-4} is obtained for fractures, compared with (Figure 2-8) 3×10^{-2} to 10^{-4} for the matrix. Thus estimates of the water vapor diffusion rates in fractures and tuff matrix overlap.

In summary, current uncertainties in water vapor diffusion rates in tuff rock span three orders of magnitude. The calculations in Section 3 with and without enhanced vapor diffusion indicate that vapor diffusion rates are quite important in estimating dryout and subsequent rewetting of the repository horizon and waste package, at least for the lower areal power density of 57 kW/acre. Additional experimental data on water vapor diffusion at elevated temperatures over a range of saturation in tuff rocks is required to reduce the uncertainty.

3 MODEL CALCULATIONS

Calculations are carried out for two-phase fluid transport using the code CTOUGH, developed at the CNWRA to replace VTOUGH (Nitao, 1988). The CTOUGH version of VTOUGH has an improved user friendly I/O, and includes an enhanced direct solver which reduces both CPU time and memory by up to factors of three or more, compared to the original VTOUGH code, when run on a Sun workstation or equivalent.

Two models of YM are used to investigate transport of liquid and vapor following emplacement of HLW. The first is based on a single-layer model using the properties of the Topopah Spring unit. The second model is based on a simplified representation of the host rock as a layered medium consisting of four different stratigraphic units. Several different computational grids are used for 1D and 2D calculations. A coarse and fine grid, of 5 and 1 m resolution in the neighborhood of the repository, are employed for 2D calculations. For the 1D calculations a much finer grid resolution is possible taken as 1 cm in the vicinity of the repository horizon.

3.1 SINGLE-LAYER MODEL

3.1.1 Input Parameters

Calculations are carried out for one- and two-spatial dimensions. In the 1D calculations, the domain of interest varies vertically from the ground surface to the water table 600 m below. In the 2D model, the domain varies radially 2 km from the repository center with the same vertical dimension as in the 1D case. The repository is assumed to lie horizontally to preserve cylindrical symmetry and is located at a depth of 225 m above the water table. In the 1D case, the repository is modeled as a point heat source. For the 2D case, it is modeled as a disk. A time-dependent heat generation rate corresponding to initial areal power densities of 57- and 114-kW/acre is used in both geometries. Ten-year-old spent fuel using mixed boiling water reactor (BWR) and pressure water reactor (PWR) fuel is used in the calculation. The equivalent continuum model is used to describe flow in the rock matrix and fracture network with the material properties given in Table 3-1. For the values of the matrix and fracture permeability and porosity given in the table, an equivalent continuum model permeability of $1.8\times10^{-14}\,\mathrm{m}^2$, and a porosity of 0.10 is obtained. These values define the base case for the calculations.

The value chosen for the fracture permeability is uncertain. For the selected values of the fracture network porosity and matrix permeability given in Table 3-1, the composite model has the range of possible permeabilities shown in Figure 3-1. For the typical case with $\varphi_f \ll \varphi_m < 1$, for $\varphi_f k_f \ll k_m$ the equivalent continuum permeability is equal to the matrix permeability k_m, and for $\varphi_f k_f \gg k_m$ is equal to the fracture permeability times the fracture porosity $\varphi_f k_f$, referred to as the continuum fracture permeability. This explains the two limiting slopes in Figure 3-1.

The relation between matrix and fracture saturation and the composite model saturation is shown in Figure 3-2 in which the logarithm of liquid saturation in the fracture and matrix is plotted as a function of the logarithm of the composite or equivalent continuum model liquid saturation. Fracture saturation becomes appreciable only when the matrix is also near fully saturated conditions. Slightly below near-full saturation, the composite model saturation is nearly identical to the matrix saturation.

The equivalent continuum model permeability and relative liquid permeability are plotted in Figures 3-3 and 3-4, respectively, for the parameters given in Table 3-1, making use of the van Genuchten relation for relative permeability as a function of saturation given in Eq. (2-26). A binary diffusion acceleration factor of unity is used in the base case. In Figure 3-3, the curve labeled matrix corresponds to the limiting case of zero fracture permeability. A typical double-humped relation is obtained for the upper two curves indicating contributions from fractures at almost fully saturated conditions. As is apparent from the figures, substantial liquid transport occurs only close to fully saturated conditions.

Table 3-1. Material properties used for the base case calculations

Property	Matrix	Fracture
$k\,[m^2]$	1.9×10^{-18}	1.0×10^{-11}
φ	0.1	0.0018
τ	0.5	0.5
$\alpha\,[Pa^{-1}]$	5.8×10^{-7}	1.315×10^{-4}
m	1.798	4.23
s_r	0.001	0.001
Rock Density $[kgm^{-3}]$	2580	N/A
Rock Specific Heat $[Jkg^{-1}C^{-1}]$	840	N/A
Thermal Conductivity $[Wm^{-1}C^{-1}]$ wet dry	 2.3 1.74	N/A
$D_{va}\,[m^2s^{-1}]$	2.5×10^{-5}	N/A

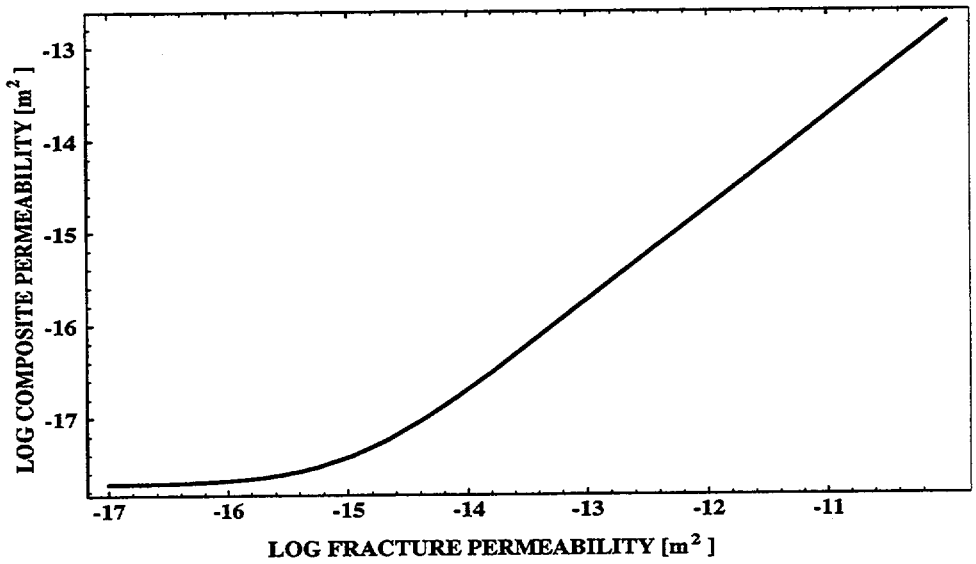

Figure 3-1. Logarithm of the composite model permeability plotted as a function of fracture permeability with porosities of matrix and fractures and matrix permeability given in Table 3-1

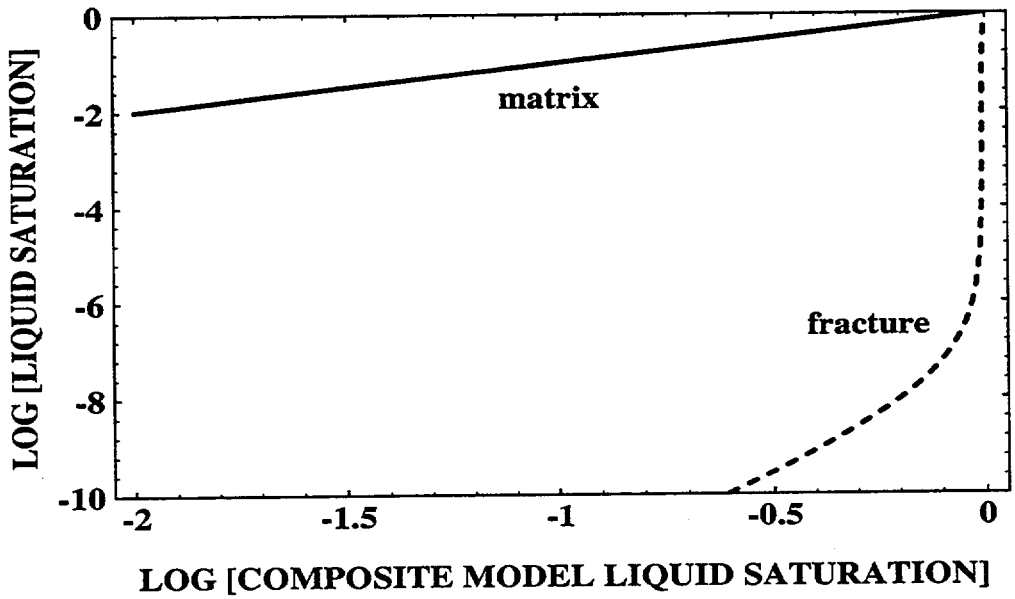

Figure 3-2. Liquid saturation in the matrix (solid curve) and fracture (dashed curve) plotted as a function of the composite model saturation based on the data in Table 3-1

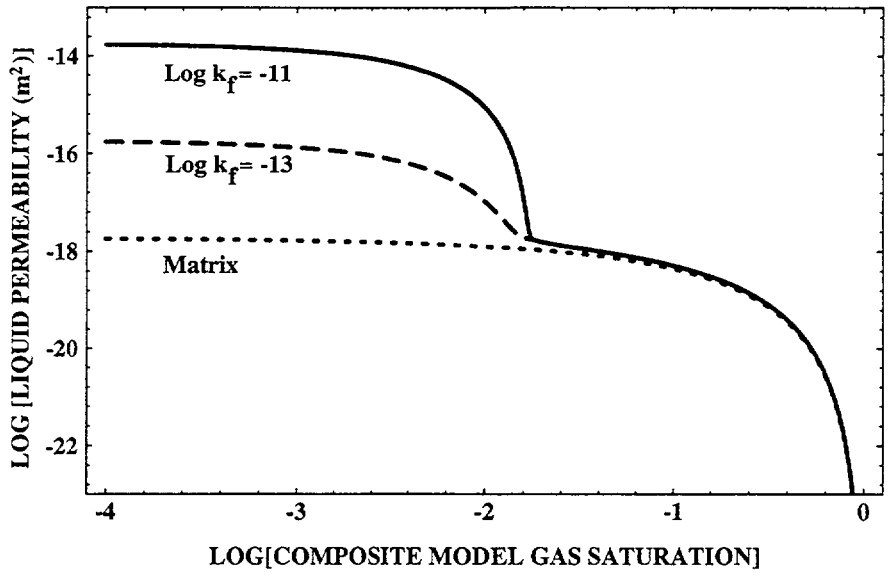

Figure 3-3. Logarithm of the equivalent continuum model permeability plotted as a function of the logarithm of the equivalent continuum model gas saturation

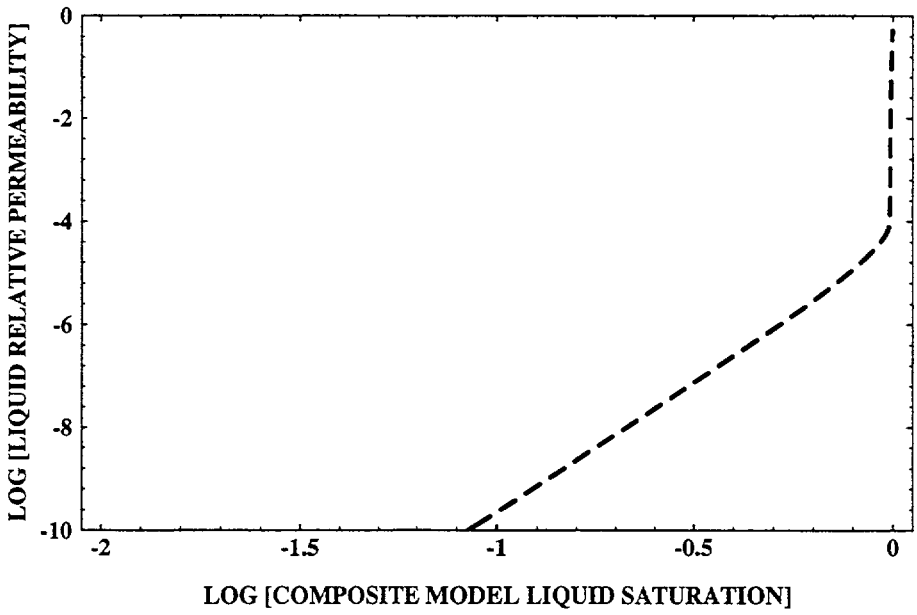

Figure 3-4. Logarithm of the relative liquid fracture permeability corresponding to the equivalent continuum model plotted as a function of logarithm of the equivalent continuum model liquid saturation

Table 3-2. Initial conditions for temperature and saturation before equilibration

Location	Temperature [°C]	Saturation
Surface	15	0.5
Water table	30	1.0

3.1.2 Initial and Boundary Conditions

Specifying appropriate initial and boundary conditions for the repository-scale model is problematic because conditions at the surface of YM vary seasonally causing the infiltration rate and liquid saturation to change with time. Using an average value may not provide a realistic description. Furthermore, the equivalent continuum model, because of the condition of capillary equilibrium between fractures and matrix, may not be able to represent adequately infiltration rates. For infiltration rates larger than the hydraulic conductivity of the equivalent continuum, a wetting front propagates downward at a velocity given by

$$v_{\text{infil}} = \frac{v_0}{[\varphi_f + (1-\varphi_f)\varphi_m](1-s_l)}, \tag{3-1}$$

where v_0 denotes the infiltration rate. This infiltration velocity is much smaller, by orders of magnitude, than the velocity which would be attained from fracture flow only in the absence of imbibition. For the Topopah Spring unit, the hydraulic conductivity is on the order of 0.05 mm/yr. For an infiltration rate on the order of 1 mm/yr, it would take about 20,000 yr for the wetting front to reach the repository with a porosity of 0.1 and liquid saturation of 0.5, according to the equivalent continuum model.

Specifying the saturation at the boundary, equivalent to a fixed head boundary condition, implies a nonzero infiltration flux. However, the value of the flux is extremely small, and there is expected to be little difference between assuming zero flux or fixed saturation boundary conditions. At the water table, the saturation is taken as unity, and the temperature is set by the geothermal gradient. This latter condition is not considered necessarily realistic, however, because considerable heating of the groundwater below the water table is to be expected following emplacement of waste. It does represent one of a number of possible endmember cases corresponding to the situation in which the groundwater flow velocity is sufficiently fast to cool the rock and keep it at a constant ambient temperature at depth. However, the temperature variation at the water table is probably only a second-order effect sufficiently close to the repository. For the 2D calculations, zero flux boundary conditions were used at a radial distance of 2 km from the repository center.

It is essential to calculate the initial conditions by equilibrating the solution with fixed saturation and temperature boundary conditions in the absence of a radiogenic heat source. This procedure provides an initial distribution of moisture which varies vertically within the mountain. To do this, boundary conditions corresponding to fixed temperature and liquid saturation at the surface and water table given in Table 3-2 were used. The temperature is assumed to vary linearly with depth to represent a geothermal isotherm.

Initially, before equilibration, the liquid saturation is assumed to vary linearly with depth. The pressure is assumed to be 1 bar throughout. An equilibration calculation was performed without a heat source present and the calculation was run out to 10 M yr. This established a dynamic steady-state with nonzero vapor and liquid fluxes. The equilibrated saturation profile and liquid and vapor velocities are shown in Figures 3-5 and 3-6. A liquid velocity of 1.5×10^{-12} m/s corresponds to approximately 0.047 mm/yr, on the order of magnitude of the recharge expected for average rainfall in the YM region. The result of this calculation is used as the initial condition for the calculation with the repository heat source present. This step was necessary in order to obtain reasonable results for the vapor flux. If unequilibrated initial conditions were used, shown by the dotted curve in Figure 3-5, vapor moved downward rather than upward at long times with the repository in place. Given the long equilibration time that is required, on the order of 10,000,000 yr, this is not surprising since significant heat is generated by the repository for times less than 10,000 yr, much less than the time required to obtain a steady-state. It should be noted that the equilibrated initial conditions are not intended to correspond to the actual conditions at YM prior to the emplacement of nuclear waste, but only to provide a self-consistent solution.

3.1.3 57-kW/acre APD Initial Heat Load

In this section, a repository a loading of 57-kW/acre APD is considered. The base case uses the parameters listed in Table 3-1. The temperature profile plotted for different times ranging from 10 to 50,000 yr is shown in Figure 3-7. The near-linear profiles for times greater than 500 yr indicate quasi steady-state transport of heat by conduction. The maximum temperature reached is just above boiling at the repository horizon at 225 m above the water table, under 1 bar of pressure. However, because of the effect of vapor pressure lowering, boiling does not actually occur. The fixed boundary conditions at the surface and water table are apparent from the figure. The thermal perturbation produced by the radioactive waste extends from the surface to the water table and persists for over 10,000 yr.

The liquid saturation profile is plotted in Figure 3-8 at the indicated times in the near-field region of the repository extending from 150 to 300 m above the water table. Outside this region the saturation is very close to ambient conditions. A sharp dip in the liquid saturation occurs at the repository horizon where drying begins resulting from the thermal field of the repository. The saturation level falls to approximately 20 percent at 100 yr and then begins to increase as the repository cools..

Shown in Figures 3-9 and 3-10 are the temperature and liquid saturation plotted as a function of time for several different heights above the repository of approximately 0, 10, 20, 50, 100, and 200 m. Although the temperature rises above boiling, boiling does not occur because of vapor pressure lowering. Liquid saturation at the repository horizon is essentially restored after several thousand years have elapsed

The sensitivity of the calculations to vapor pressure lowering and enhanced vapor diffusion are investigated next. Liquid saturation profiles are compared with the base case in Figure 3-11 in the absence of vapor pressure lowering and with enhanced vapor diffusion for an elapsed time of 100 yr. The solid curve refers to the base case, the dashed curve to enhanced vapor diffusion, and the dotted curve to the absence of vapor pressure lowering. In the absence of vapor pressure lowering, boiling with complete dryout occurs in the vicinity of the repository. Enhanced vapor diffusion leads to a much larger region of reduced liquid saturation, but complete dryout does not occur. Neither vapor pressure lowering nor enhanced vapor diffusion have any noticeable effect on the temperature profile which is conductive dominated.

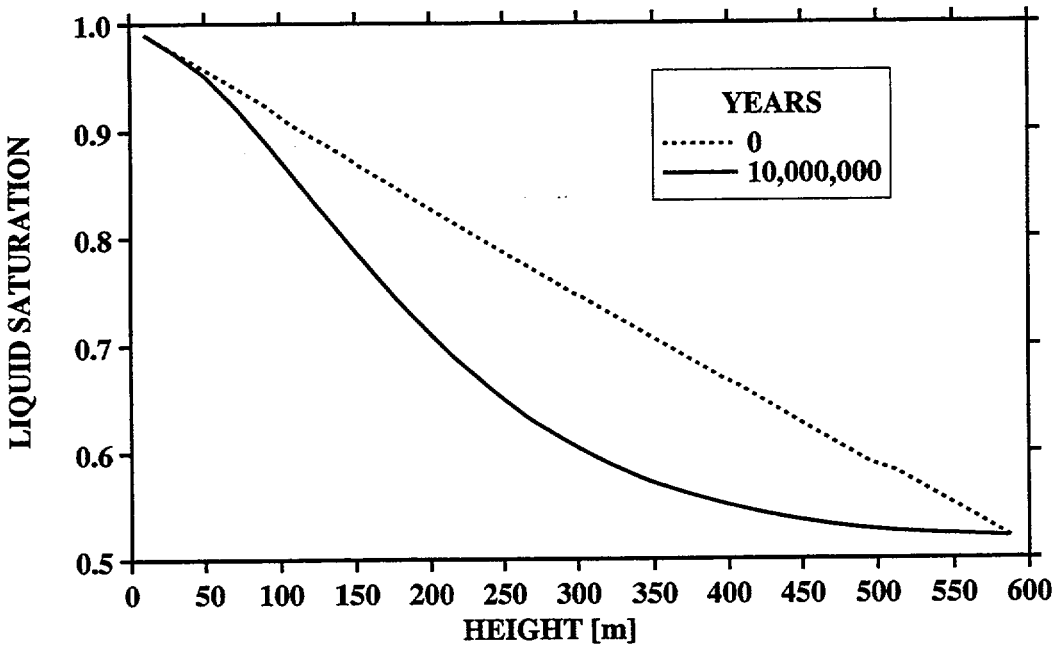

Figure 3-5. Liquid saturation profile for the equilibrated initial conditions (solid curve) plotted as a function of the height above the water table

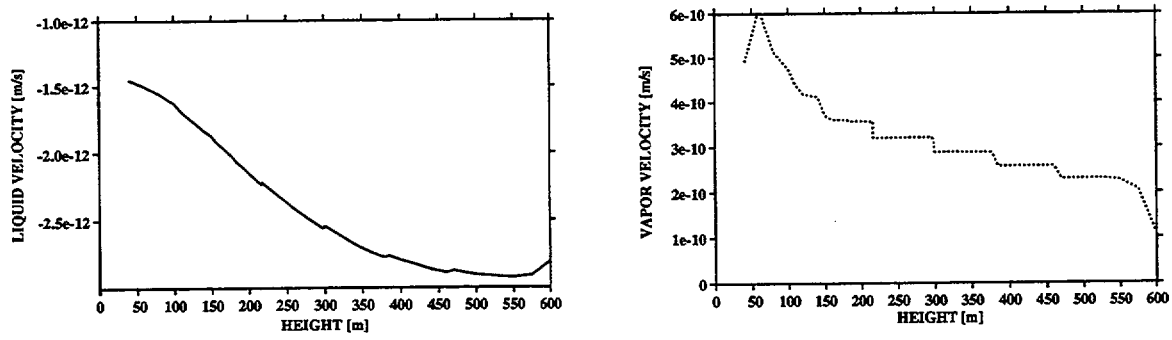

Figure 3-6. Average liquid and vapor pore velocities corresponding to the equilibrated initial conditions. A positive velocity indicates upward movement and a negative velocity, downward.

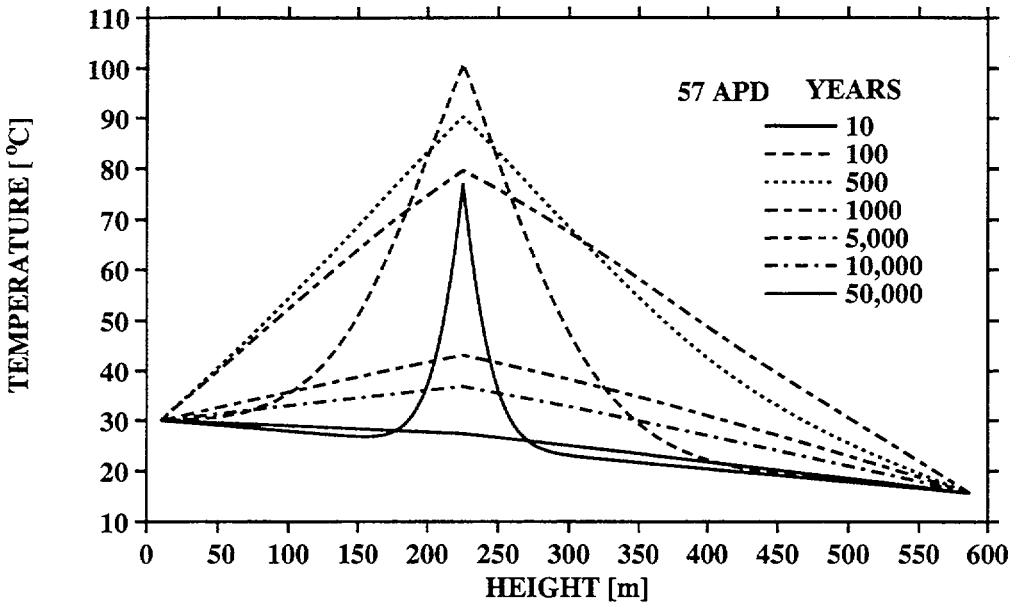

Figure 3-7. Temperature profiles for the 57-kW/APD loading base case plotted at the indicated times

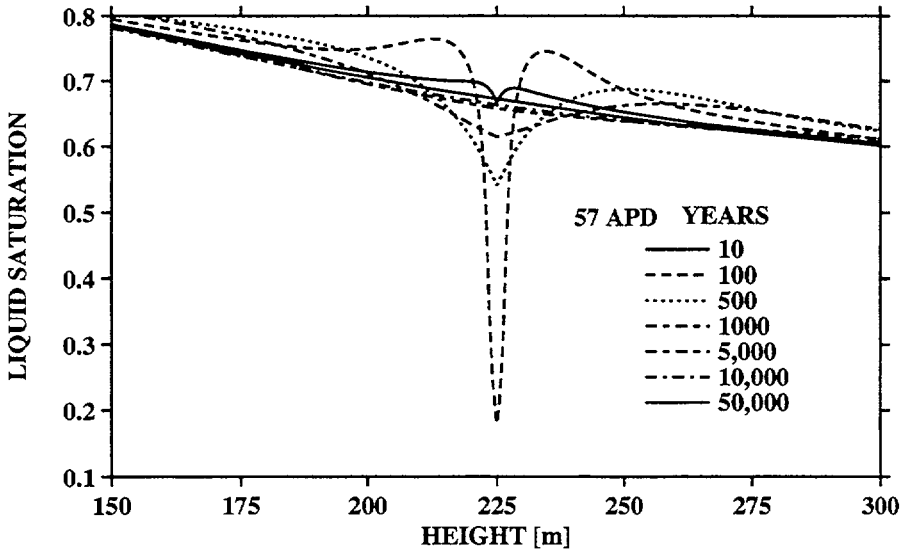

Figure 3-8. Liquid saturation profiles for the 57-kW/APD loading base case plotted at the indicated times

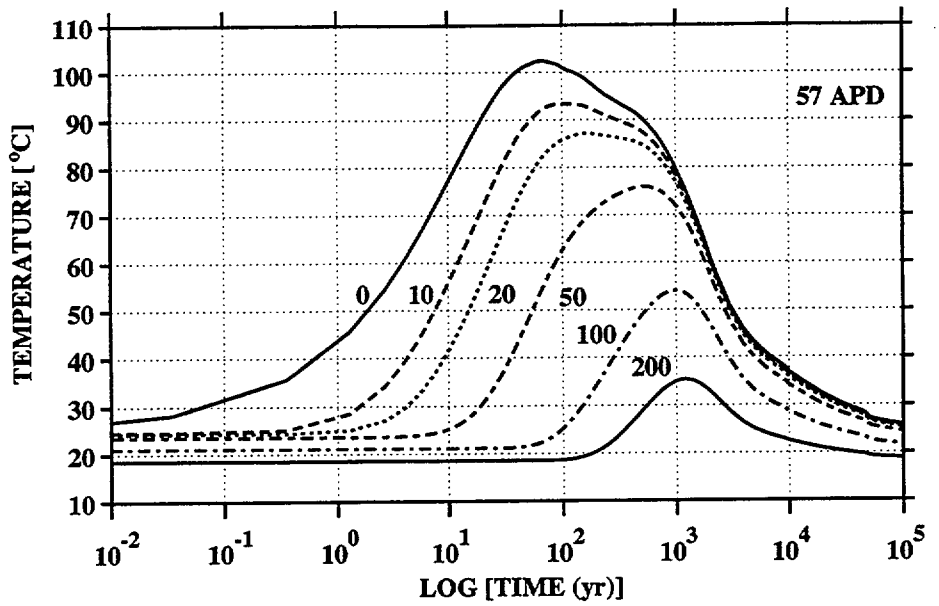

Figure 3-9. Temperature plotted as a function of time for several different heights (m) above the repository

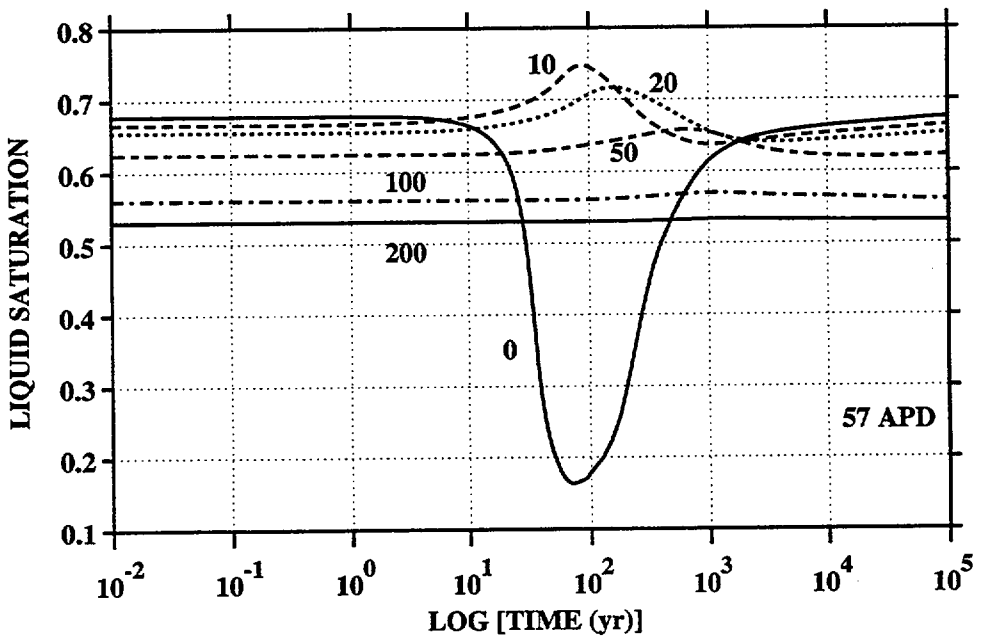

Figure 3-10. Liquid saturation plotted as a function of time for several different heights (m) above the repository

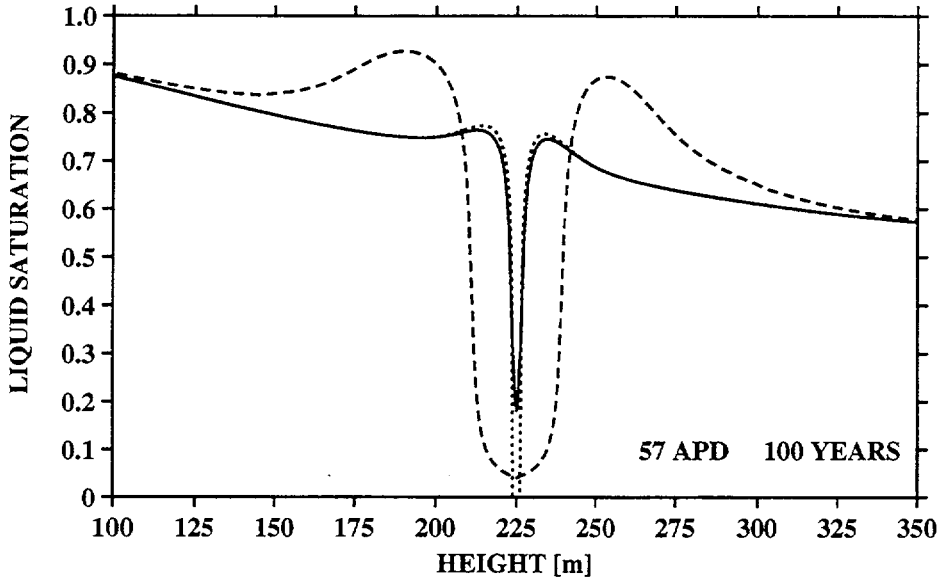

Figure 3-11. Comparison of liquid saturation profiles for the 57-kW/APD loading base case (solid curve) for an elapsed time of 100 yr without vapor pressure lowering (dotted curve), and with enhanced diffusion (dashed curve)

The effect of vapor pressure lowering and enhanced vapor diffusion on the liquid and gas flux is shown in Figures 3-12 and 3-13. The solid and dotted curves refer to liquid and vapor fluxes, respectively, for the base case. The dashed and dashed-dotted curves refer to the liquid and gas fluxes, respectively, for the cases without vapor pressure lowering and with enhanced vapor diffusion. Notice the different length scales used to construct the two figures. With the exception of enhanced vapor diffusion, the liquid and vapor fluxes are equal in magnitude, but opposite in direction indicating quasi-steady behavior. In all cases, sufficiently close to the repository horizon, below the repository liquid moves upward and vapor downward, whereas above the repository just the reverse takes place with liquid moving downward and vapor upward. Thus, within a narrow region of about 10 m above and below the repository, liquid moves toward the repository and vapor moves away. Liquid is drawn toward the repository by strong capillary suction forces as the immediate near-field region dries out. For the case of enhanced vapor diffusion, a much greater vapor flux is obtained with vapor clearly moving upward across the repository horizon. A change in sign occurs in the liquid flux where condensation of vapor takes place.

Tsang and Pruess (1987) attributed the cause of downward vapor movement below the repository to binary diffusion. With the diffusion mechanism shut off, vapor moved upward due to buoyancy effects. However, as demonstrated in the next section for the case of 114-kW/acre APD, binary diffusion plays only a minor role. Nevertheless, even in this case, vapor moves downward below the repository horizon, presumably as a consequence of boiling effects.

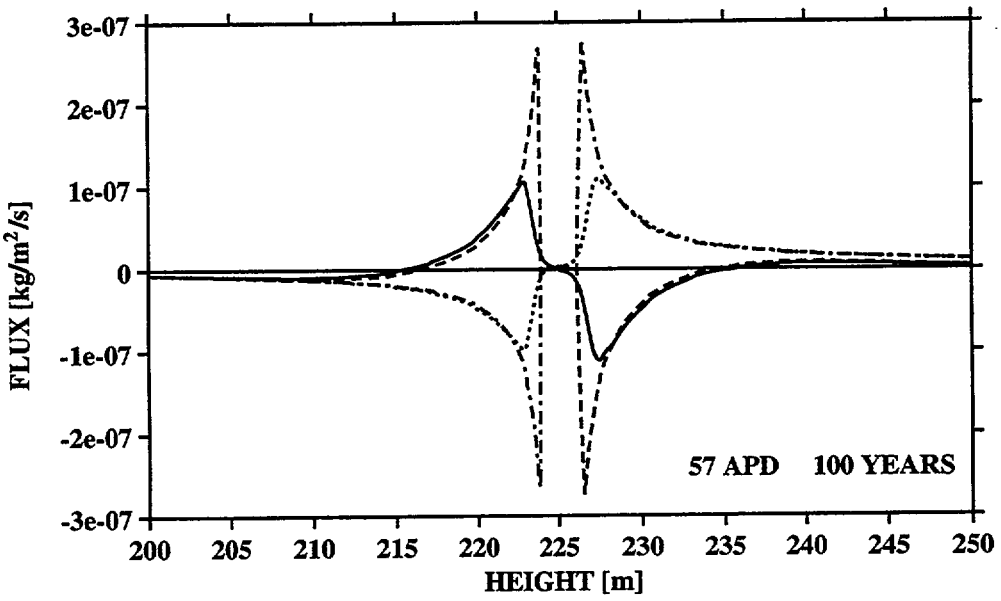

Figure 3-12. Comparison of flux profiles for the 57-kW/acre APD loading base case in the absence of vapor pressure lowering for an elapsed time of 100 yr (see text for explanation of curves)

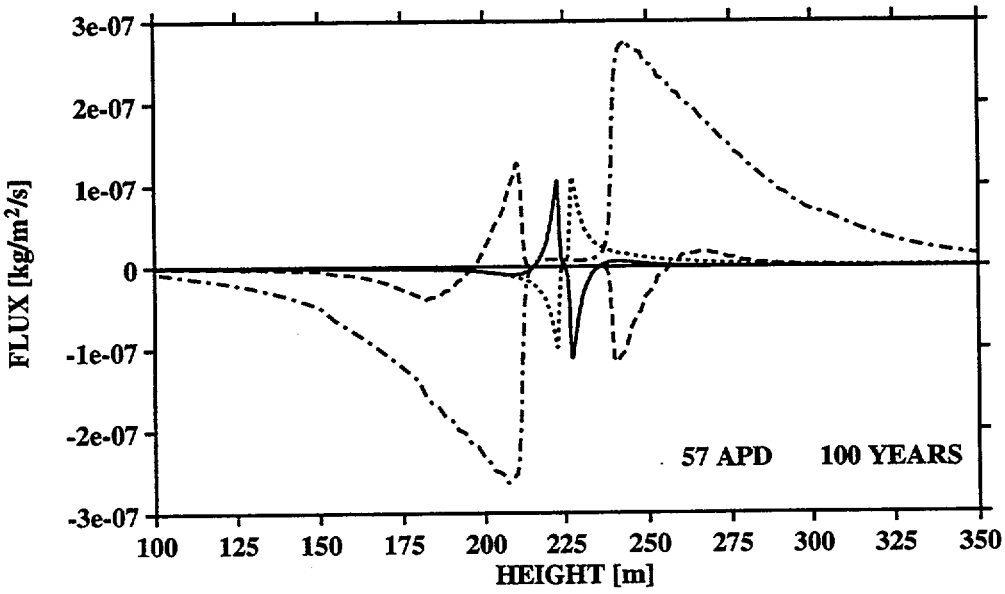

Figure 3-13. Comparison of flux profiles for the 57-kW/acre APD loading base case for enhanced vapor diffusion for an elapsed time of 100 yr with enhanced vapor diffusion (see text for explanation of curves)

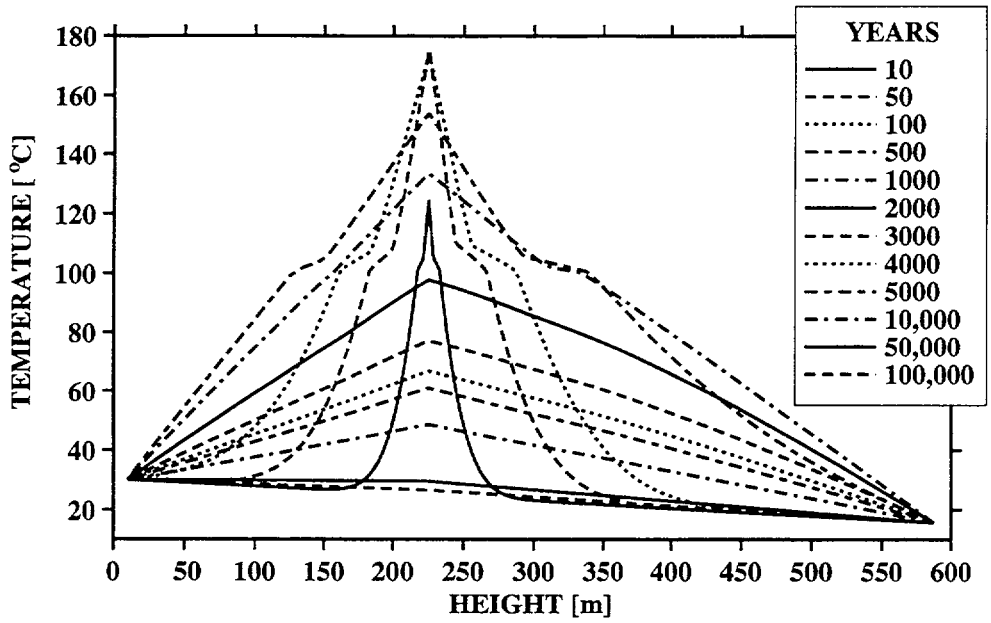

Figure 3-14. Temperature profiles at different times indicated in the figure plotted as a function of height above the water table. The existence of heat-pipes is visible in the figure for times less than 2,000 yr as gently sloping flanks of approximately constant temperature bordering the peak at the repository level.

3.1.4 114-kW/acre APD Initial Heat Load

Next, the case for an areal power loading of 114-kW/acre is considered. The calculations use the parameter values given in Table 3-1 which defines the base case. The temperature evolution for times up to 100,000 yr is plotted in Figure 3-14 as a function of the height above the water table. The maximum temperature reached is approximately 180 °C at the repository level. Particularly noteworthy in the figure is the gently sloping plateau formed immediately adjacent to the peak in temperature for times up to 1,000 yr indicative of the formation of a heat-pipe. Two heat-pipes occur, one above and one below the repository. Heat-pipe effects persist for times between approximately 1,000 and 2,000 yr. Within the heat-pipe, vigorous counter-flow of vapor and liquid water phases occurs as discussed more fully below (see Figure 3-19). For times longer than 2,000 yr the system has cooled below the boiling point of water, and a heat-pipe can no longer be sustained. In this regime the temperature profile becomes purely conduction dominated. After 100,000 yr the repository has completely cooled, and the initial ambient temperature profile is regained.

The evolution of the liquid saturation profile with time is shown in Figure 3-15. During the early stages of the evolution of the system, boiling occurs with the formation of heat-pipes drying out the rock in the vicinity of the repository. The evaporated water condenses above and below the repository creating islands of enhanced water content, as shown in the figure. Because of gravity effects, more water condenses below the repository than above it. As time increases, the islands of enhanced water content

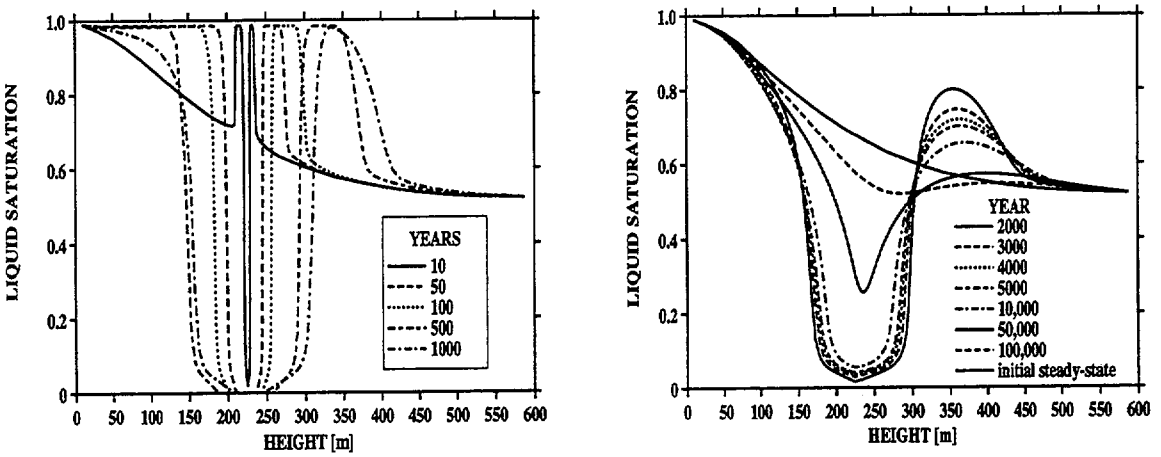

Figure 3-15. Liquid saturation profiles for times ranging from 10 to 100,000 yr. Complete dryout in the near-field of the repository is apparent for early times.

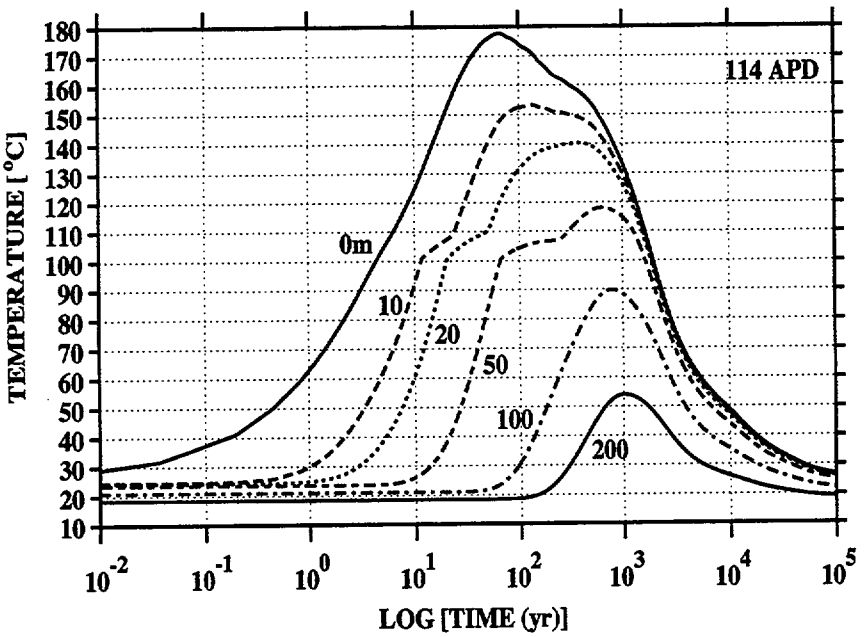

Figure 3-16. Temperature plotted as a function of time for different heights (m) above the repository

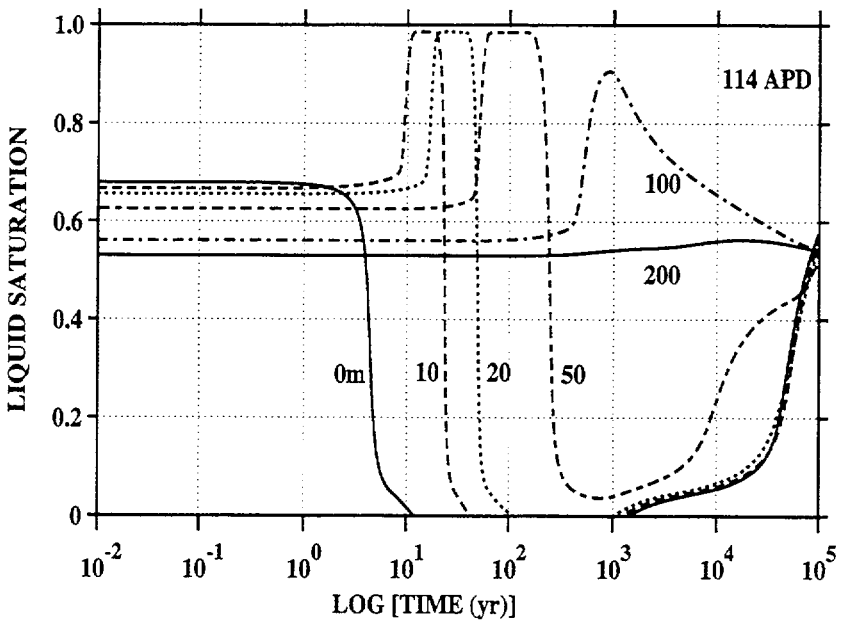

Figure 3-17. Liquid saturation plotted as a function of time for different heights (m) above the repository

move upward and downward away from the repository until the temperature drops sufficiently below the boiling point and rewetting of the repository begins. The rewetting process is much slower than the drying out process. Even after an elapsed time of 100,000 yr, the near-field region of the repository has not completely regained the ambient equilibrium saturation.

The temperature and liquid saturation are plotted in Figures 3-16 and 3-17 as a function of time for different heights above the repository. Rewetting begins after approximately 2,000 yr, but saturation increases relatively slowly until after approximately 30,000 yr, after which a sharp rise in saturation occurs.

3.1.4.1 Heat-Pipe Regime

The heat-pipe, because of its relatively long lifetime of a little over 1,000 yr for an APD of 114 kW/acre, is an important factor in determining the behavior of moisture distribution in the near-field region of the repository. Reducing the repository APD would decrease the heat-pipe lifetime. The permeability is also an important factor in determining conditions favorable for formation of a heat-pipe. This section examines more closely the properties of the heat-pipe and its effect on the near-field. Results are also compared for 1D and 2D simulations.

The temperature profile in the near-field is shown in Figure 3-18a for an elapsed time of 10 yr. The solid curve refers to the 1D model, the dashed and dotted curves to the 2D, *r-z* repository-scale model with cylindrical symmetry. The dashed curve corresponds to a finer grid compared to the dotted curve. The liquid saturation is shown in Figure 3-18b. Note that the finer grid approximates the 1D result is more

closely compared to the coarse grid. The presence of heat-pipes centered, respectively, at approximately 230 and 220 m above and below the repository is evident. The presence of heat-pipes is also apparent in Figure 3-18c in which the evaporation rate is plotted as a function of the height above the water table. A positive value of the evaporation rate represents condensation and a negative value evaporation. The peaks in the evaporation rate correspond to the ends of the heat-pipe. At one end of the heat-pipe, evaporation occurs and at the other, condensation. As the grid spacing tends to zero, the peaks become singular points approaching Dirac delta functions. The 2D calculations do a much poorer job of representing the peaks in the evaporation rate because of the much coarser grid used. The liquid and vapor flux that is shown in Figure 3-18d for the 1D case only. The solid curves correspond to liquid and the dashed curves to vapor fluxes. The presence of the heat-pipes can be identified as the regions in which counter-flow of liquid and vapor occur. Within both heat-pipes, liquid moves toward the repository as a consequence of strong capillary forces in the dried out zone despite the presence of gravity. Vapor moves away from the repository in each heat-pipe.

It will be noted that the counterflow of vapor and liquid is not balanced. At each of the heat-pipe boundaries where there is a sharp change in flux, the jump in the liquid and vapor flux across the front obeys the equation

$$[F_l + F_v] = 0 \quad , \tag{3-2}$$

where the square brackets denote the jump across the front of the enclosed quantity defined as

$$[F] = F^{(plus)} - F^{(minus)} \quad , \tag{3-3}$$

with (plus) referring to the upstream side of the front and (minus) to the downstream side. Equation (3-3) is a consequence of conservation of mass and the continuity of the field variables pressure, temperature, and saturation across the heat-pipe boundaries. At the uppermost boundary of the upper heat-pipe, complete return of the liquid phase does not occur. Furthermore, the vapor and liquid fluxes are not equal in magnitude. At the lowermost boundary of the lower heat-pipe, a smaller fraction of liquid is returned to replenish the heat-pipe. The remaining liquid travels downward toward the water table. Both above the upper heat-pipe and below the lower heat-pipe, liquid is moving away from the repository. Above the upper heat-pipe, liquid water is drawn upward by capillary suction due to the decrease in saturation. Below the lower heat-pipe, liquid water flows downward as a consequence of gravity. Note that the vapor flux does not vanish within the dryout zone in the immediate vicinity of the repository. Vapor moves downward across the repository horizon from the upper heat-pipe to the lower one. This result cannot be explained by binary diffusion, as in the previous case of the 57-kW/acre heat load. In fact, at the high heat load diffusion has only a minor effect on the vapor flux for these calculations. Most likely the result is due to a combination of boiling and because of the formation of a perched zone that is almost fully saturated above the repository, thus blocking the flow of vapor.

With increasing time, the heat-pipes separate, moving farther away from the repository horizon and increase in width as shown in Figure 3-19 in which the vapor and liquid flux is plotted for different times ranging from 10 to 1,000 yr. After 1,000 yr, the upper heat-pipe has moved approximately 65 m above the repository, and the lower heat-pipe 55 m below the repository. Complete dryout occurs between the heat-pipes. However, there is a steady downward movement of vapor across the repository horizon.

These results may be compared with the 2D model. The vapor and liquid flux is shown in Figure 3-20 for the fine and coarse grids for an elapsed time of 10 yr and, similarly, in Figure 3-21 for 50 yr. Very different results are obtained for the coarse and fine grids. The finer grid agrees more closely with the 1D calculations compared to the coarser grid. At 50 yr elapsed time, the fine grid 2D calculation also predicts downward flow of vapor in agreement with the 1D calculation shown in Figure 3-22. If this result is correct, this prediction could have significant implications for transport of carbon-14 from the repository.

The 1D flux profile is compared with the 2D case for 50 yr in Figure 3-22. Excellent agreement is obtained between the two models indicating that, at least near the center of the repository, it should be possible to use a single spatial dimension for understanding the near-field behavior of the repository. For longer time spans, after the waste heat has substantially decayed, it might be expected that such good agreement would not be obtained. This issue is addressed in Section 3.1.4.2 on the rewetting phase of the repository. It should also be kept in mind that in these calculations the repository is assumed to lie horizontally and, thus, gravity acts perpendicular to the plane of the repository disk. For a tilted repository, 2D effects may become more important.

It is clear from the figures in Pruess and Tsang (1994) that a relatively coarse grid was used in their calculations. By contrast, in the 1D calculations, an extremely fine grid is used which results in smoothly varying results in which placement of the grid points is not obvious from the figure itself, as it is in Pruess and Tsang (1994). As the comparison with the coarse grid 2D calculation has shown, if a sufficiently fine grid is not used, misleading results can be obtained.

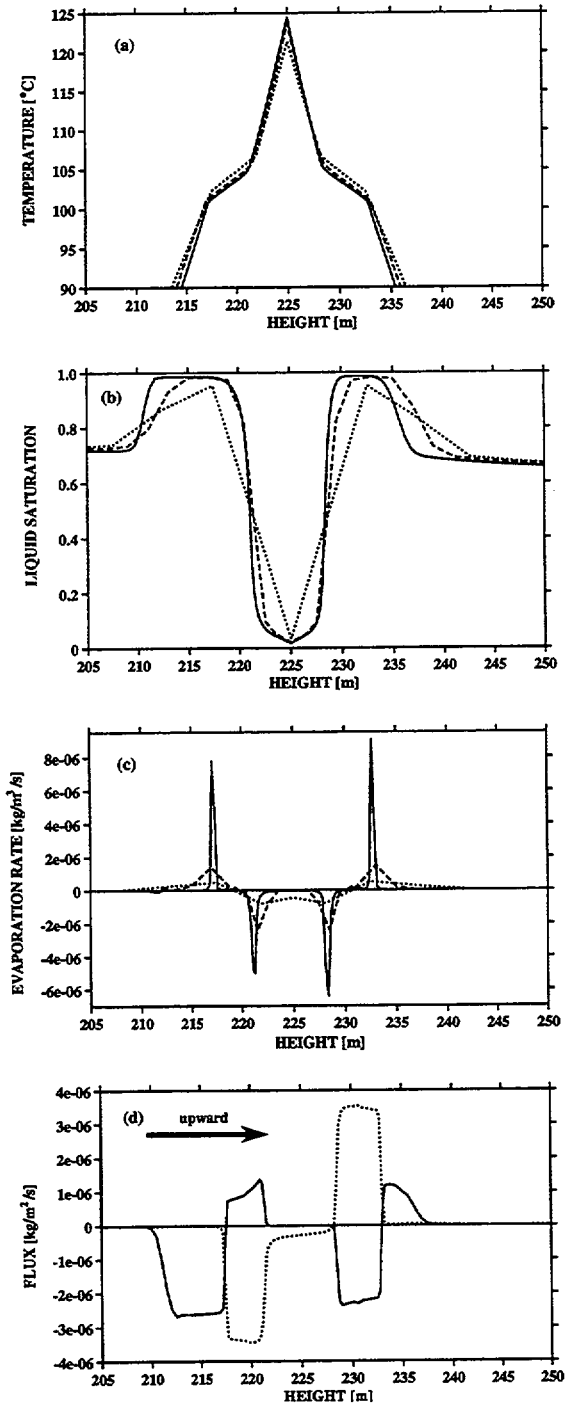

Figure 3-18. Profiles for (a) temperature, (b) liquid saturation, (c) evaporation rate, and (d) liquid and vapor flux profiles, plotted as a function of the height above the water table for an elapsed time of 10 yr. In figures (a), (b), and (c) the solid curve refers to the 1D calculation, and the dashed and dotted curves to the 2D results with a fine and coarse grid, respectively. In the lower plot the dotted curve refers to vapor and the solid curve to liquid flux.

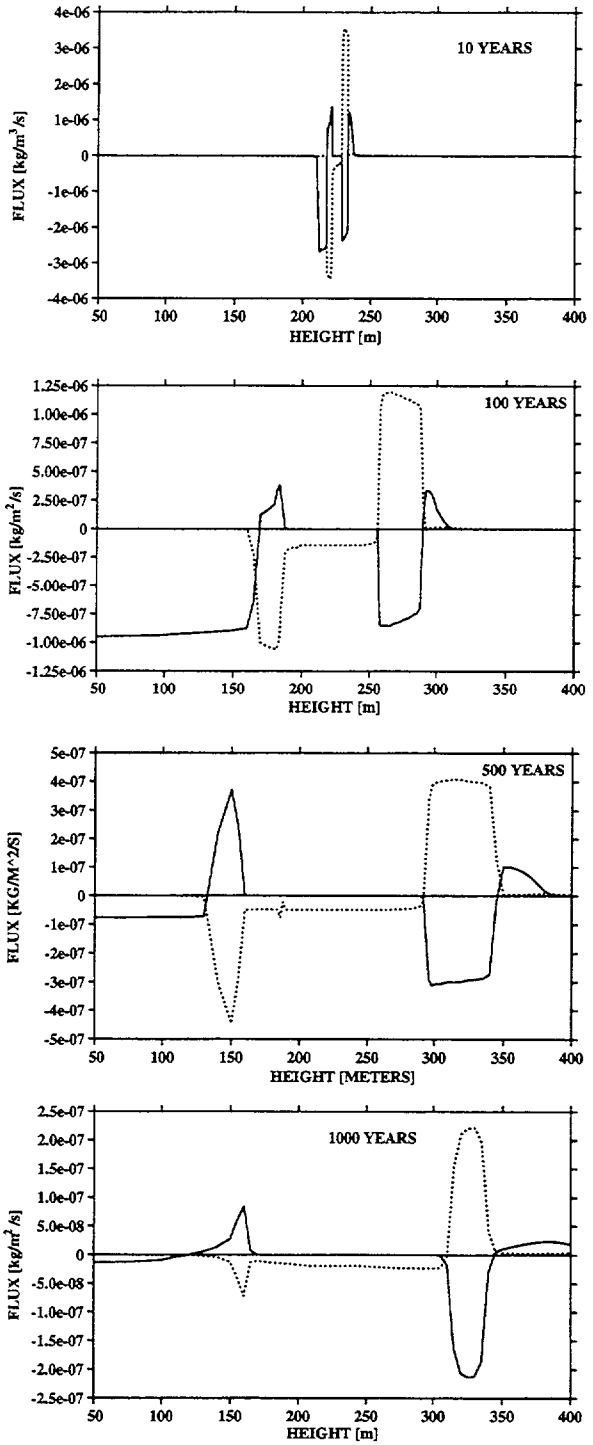

Figure 3-19. Evolution of heat-pipe with time showing the liquid and vapor flux at the indicated times plotted as a function of height above the water table. The downward transport of vapor across the repository horizon from the upper to lower heat-pipe is clearly visible.

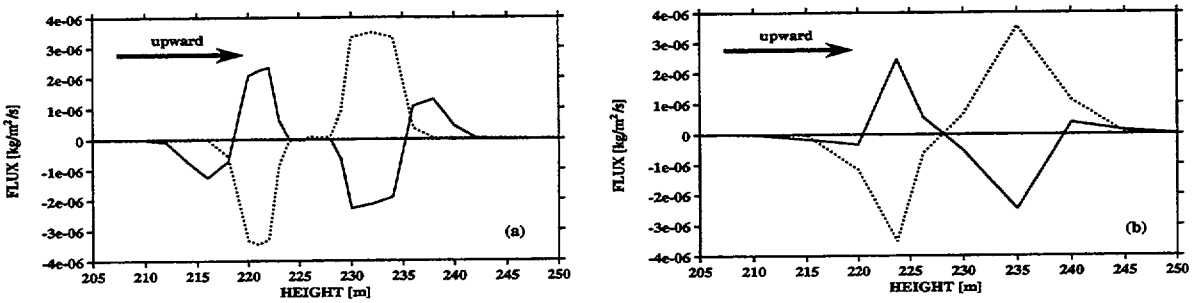

Figure 3-20. 2D repository-scale model using (a) fine and (b) coarse grids for an elapsed time of 10 yr

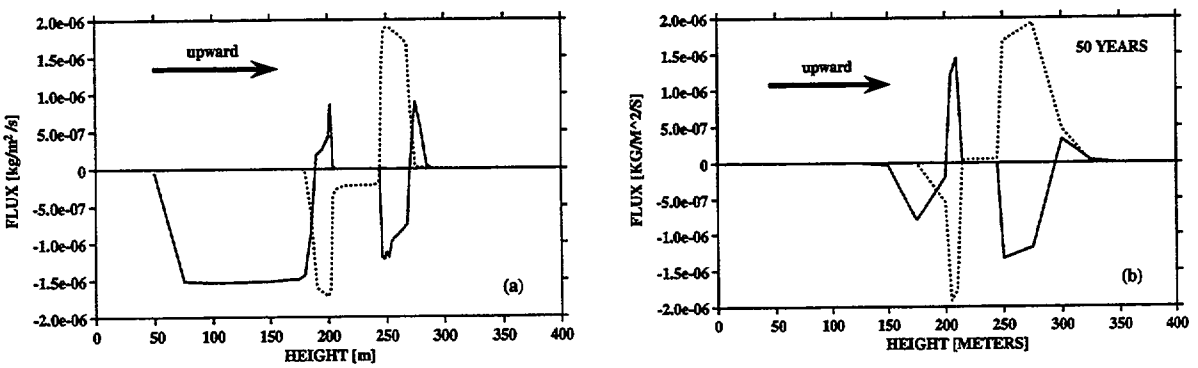

Figure 3-21. 2D repository-scale model using (a) fine and (b) coarse grids for an elapsed time of 50 yr

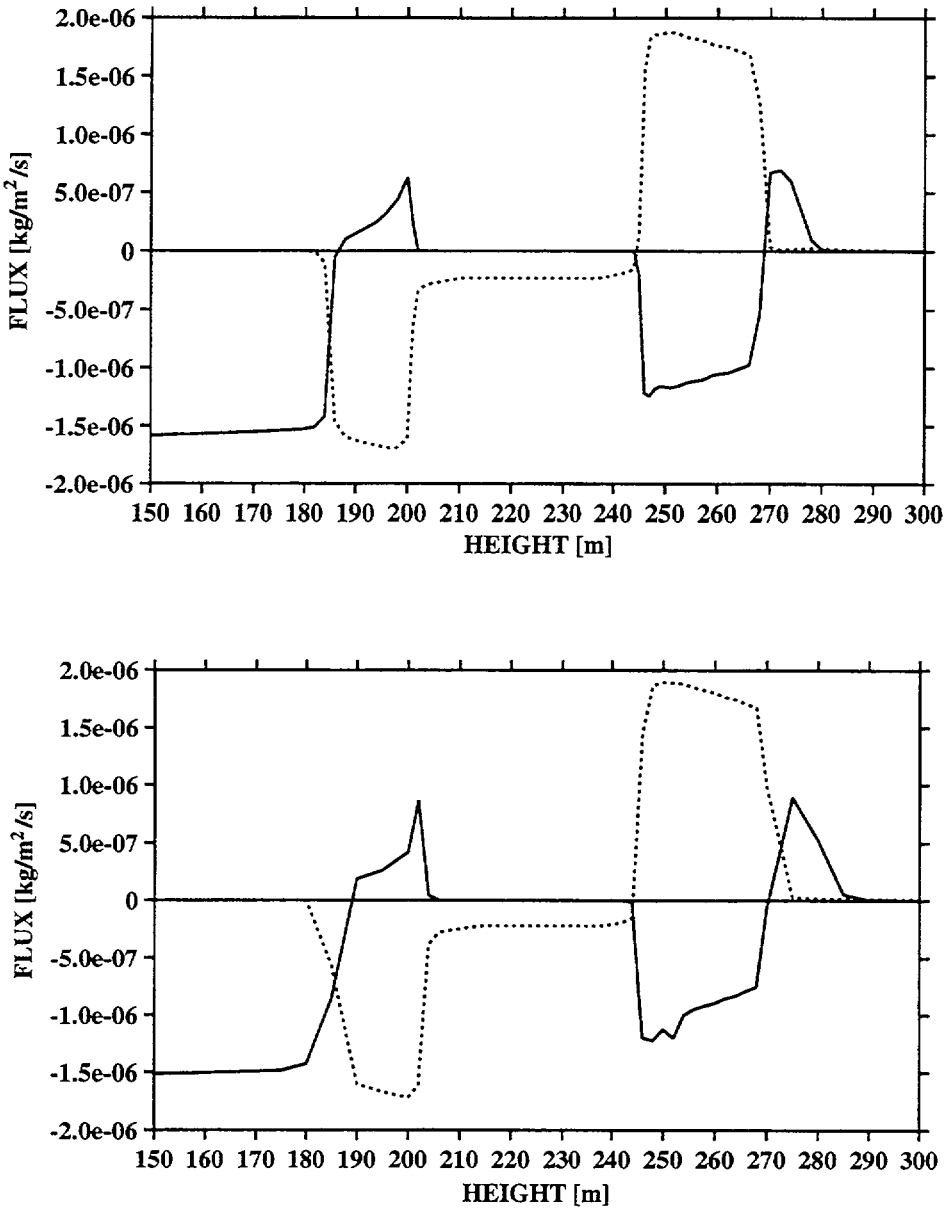

Figure 3-22. Comparison of liquid and vapor fluxes for 1D and 2D calculations for an elapsed time of 50 yr

3.1.4.2 Rewetting Period

After the repository has cooled down sufficiently, the process of rewetting begins. Shown in Figure 3-23 is the liquid and vapor flux plotted as a function of height above the water table for times ranging from 2,000 to 10,000 yr. Both above and below the dryout zone, liquid moves toward the repository due to capillary suction. Liquid contained in the island of enhanced saturation above the repository moves both upward and downward, but eventually moves totally toward the repository. Within the dryout zone, vapor moves away from the repository. The evaporation rate is shown in Figure 3-24. As expected, condensation now occurs at the repository itself with evaporation occurring both high above and below the repository.

Comparison of 1D and 2D fluxes for long times is shown in Figures 3-25 and 3-26. Although the results are qualitatively similar, the agreement is not as good as it is for earlier times. The cause of the discrepancy could be due either to numerical problems or arise from the 2D nature of the problem. It might be expected that for long times vapor transport would be driven by large scale buoyancy effects, processes which the 1D model may not properly take into account. However, the vapor flux gives much better agreement than the liquid flux, which is somewhat surprising.

3.1.4.3 Infiltration

This section explores the limitation of the equivalent continuum model in describing infiltration. To this end, a constant rate of infiltration is imposed at the ground surface and allowed to penetrate downward toward the repository. Infiltration is assumed to commence coincidentally at the time of waste emplacement. No attempt is made to represent realistic infiltration rates that might occur at YM due to rainfall, for example. Rather, the purpose here is merely to investigate the ability and characteristic behavior of the equivalent continuum model to describe prolonged infiltration. The source of infiltration could be other than assumed here. For example, it could occur from perched zones of elevated saturation caused by condensation of vapor.

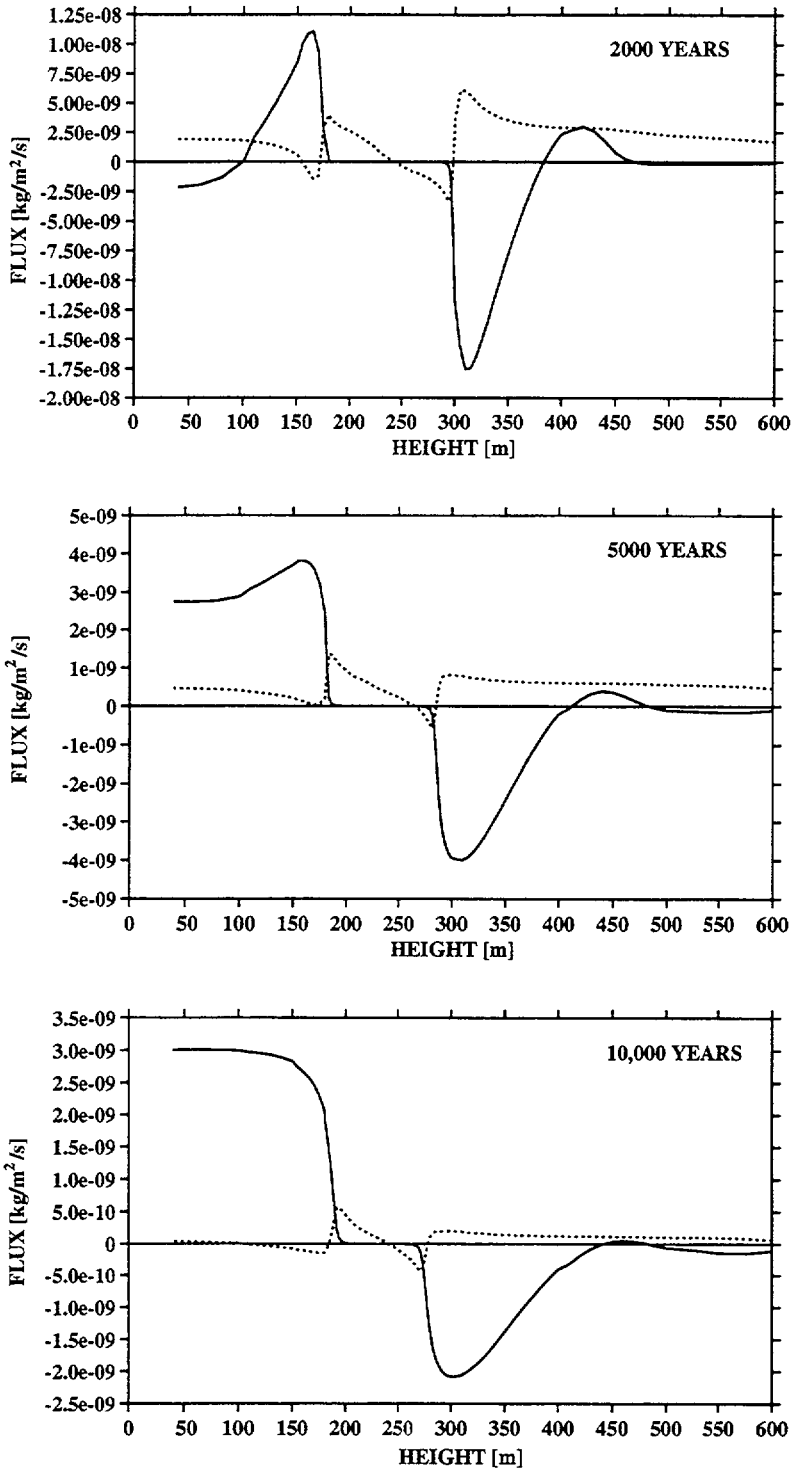

Figure 3-23. Liquid (solid curve) and vapor (dotted curve) flux at the indicated times during the rewetting period

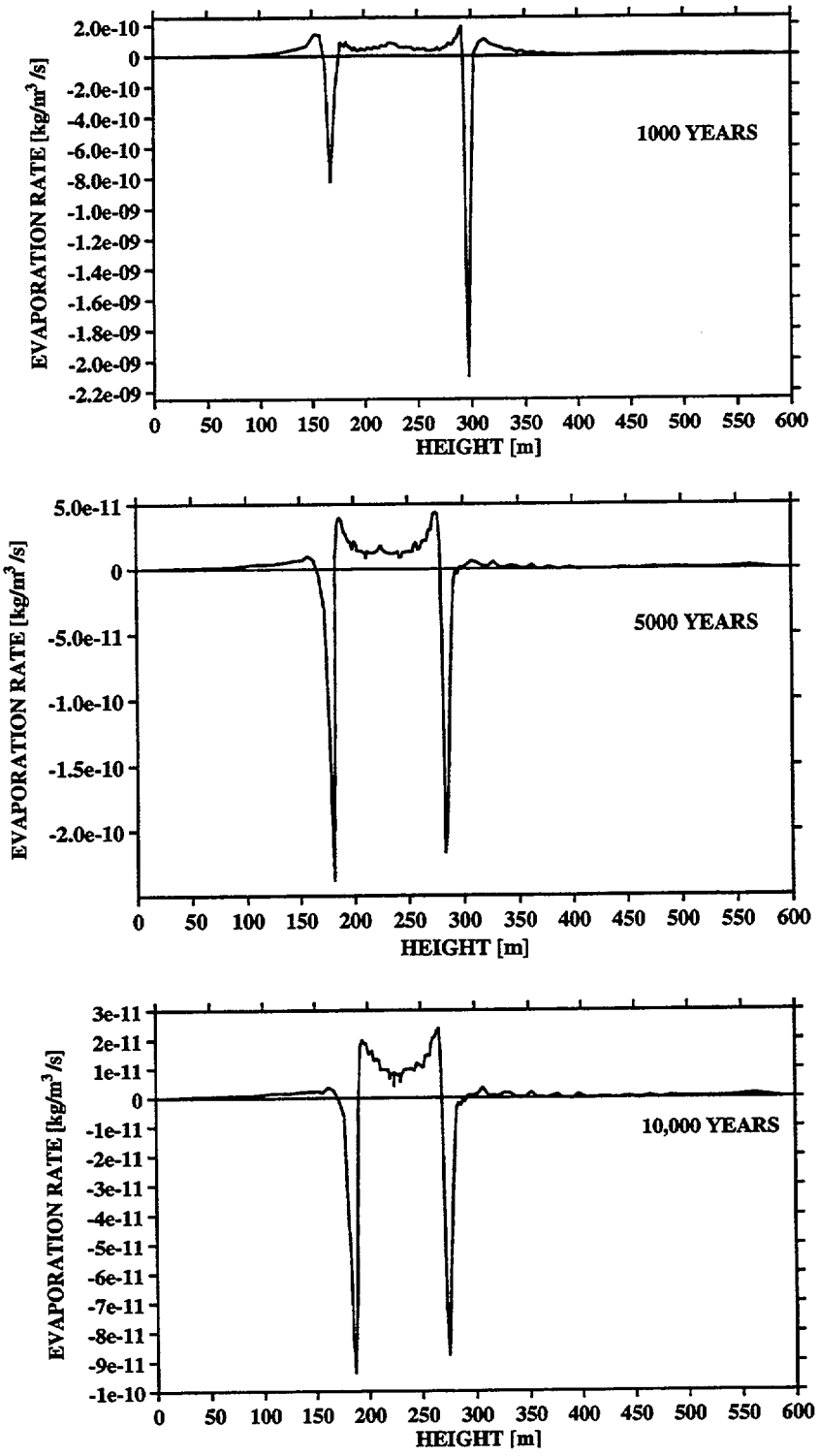

Figure 3-24. Evaporation rate plotted as a function of the height above the water table showing rewetting of the repository. Condensation is positive and evaporation is negative.

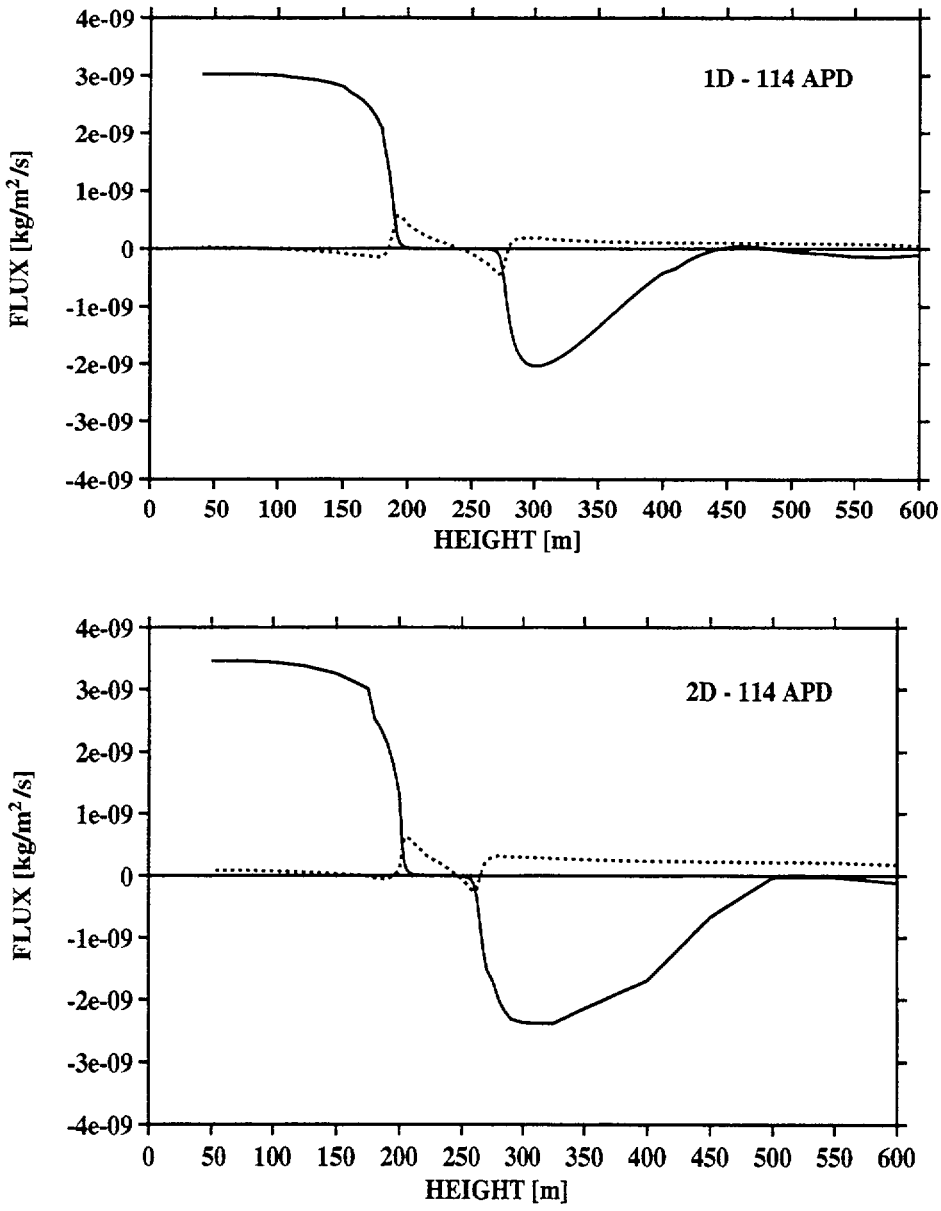

Figure 3-25. Comparison of liquid (solid curve) and vapor (dotted curve) fluxes for 1D and 2D calculations for an elapsed time of 10,000 yr

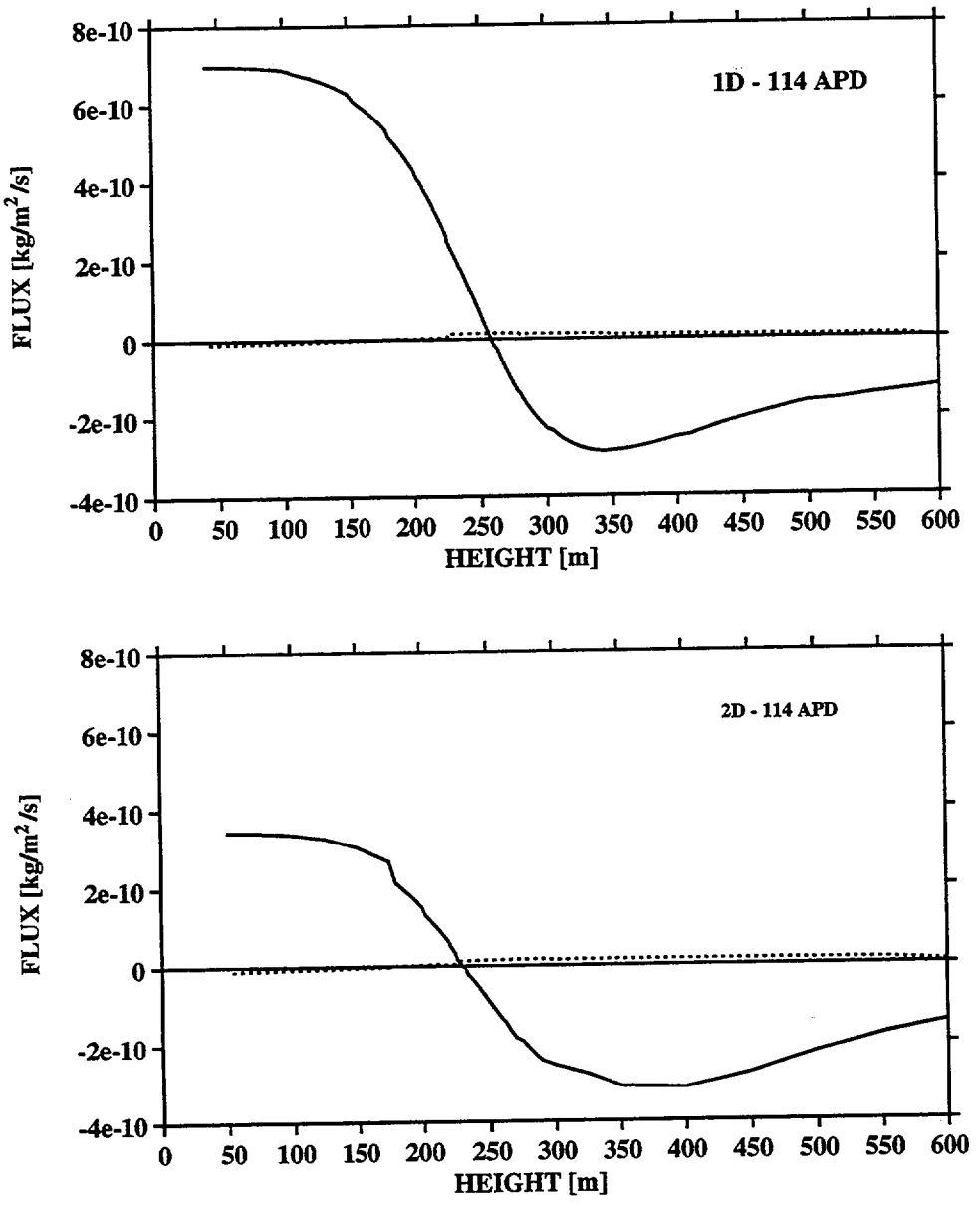

Figure 3-26. Comparison of liquid (solid curve) and vapor (dotted curve) fluxes for 1D and 2D calculations for an elapsed time of 100,000 yr

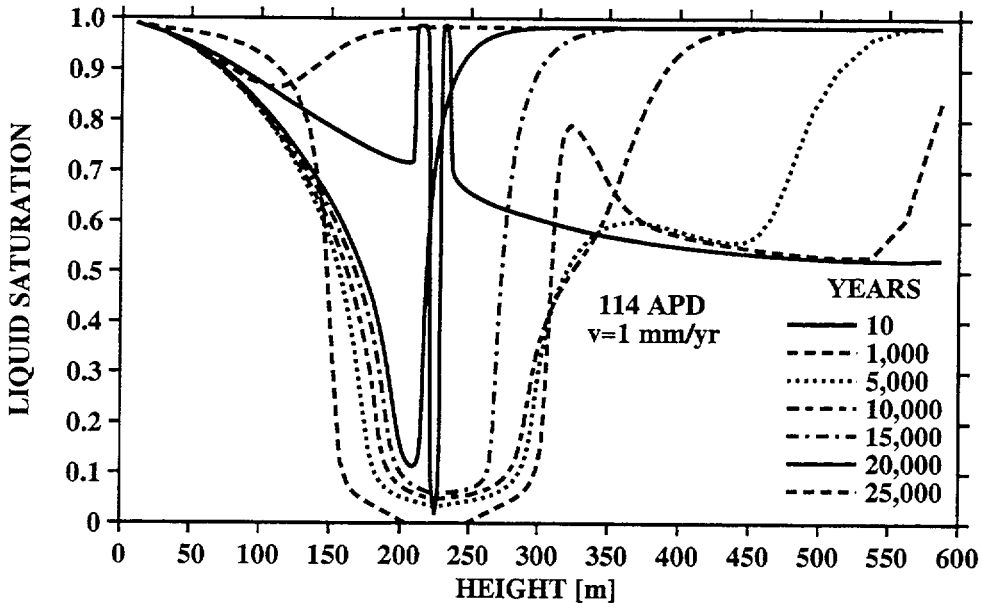

Figure 3-27. Liquid saturation profiles for the indicated times resulting from an infiltration rate at the ground surface of 1 mm/yr

Shown in Figure 3-27 is the liquid saturation profile for times ranging up to 25,000 yr for an infiltration rate of 1 mm/yr. The infiltration front propagates downward at a retarded rate given by Eq. (3-1). The time t for the front to travel a distance l is equal to

$$t = \frac{l\varphi\,(1 - s_l)}{v_0}, \tag{3-4}$$

which is in good agreement with the calculated results taking $v_0 = 1$ mm/yr, φ=0.1, and $s_l \cong 0.5$. Thus, the rate of advance of the front is limited by the volume of fluid required to fill matrix porosity. The matrix must become fully saturated before the front can advance along the fractures. If there were no imbibition, the front would travel much faster with φ in Eq. (3-4) replaced by the fracture porosity. Consequently, the equivalent continuum model could grossly underpredict propagation of liquid infiltration fronts.

3.1.4.4 Reduced Fracture Permeability

By reducing the fracture permeability the heat-pipe effect does not occur. For a fracture permeability of $1.0 \times 10^{-13}\,\mathrm{m}^2$, the composite permeability of the equivalent continuum model becomes $1.8 \times 10^{-16}\,\mathrm{m}^2$. The resulting temperature profile is shown in Figure 3-28. The absence of plateaus in the temperature profile is indicative of the absence of heat-pipes for this case. The liquid saturation profiles are shown in Figure 3-29. In this case, the near-field of the repository never completely dries out as in the

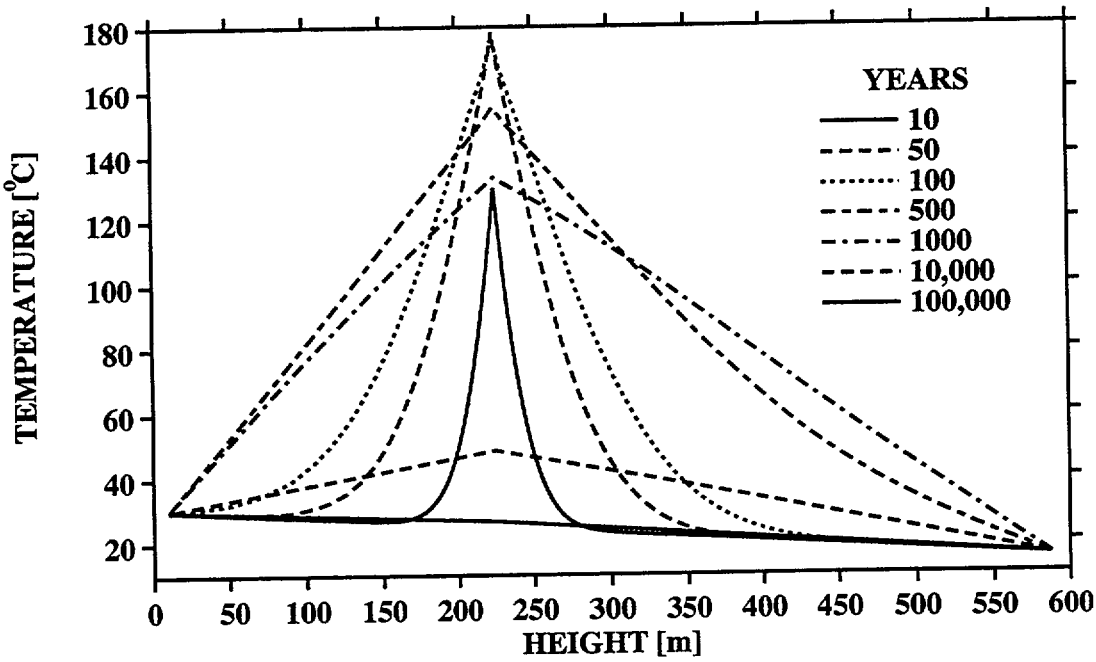

Figure 3-28. Temperature profile for the indicated times plotted as a function of height above the water table for the low-fracture permeability case

higher permeability case. The liquid and vapor flux is depicted in Figure 3-30 for times ranging from 10 to 10,000 yr. The vapor flux is away from the repository moving upward above the repository horizon and downward below it. For times less than several thousand years, the liquid flux changes sign, moving towards the repository in the vicinity of the repository and away from the repository at further distances above and below the repository. At very early times in the immediate vicinity of the repository, the liquid and vapor fluxes are equal in magnitude but opposite in sign. Vapor diffusion is a much more important process for this case of low permeability compared to the previous case of higher fracture permeability.

3.2 MULTILAYER MODEL

To investigate the effect of different stratigraphic layers on the distribution of liquid and vapor within the repository environment following emplacement of HLW, a multilayer model is used. Two heat loads of 57-and 114-kW/acre are considered.

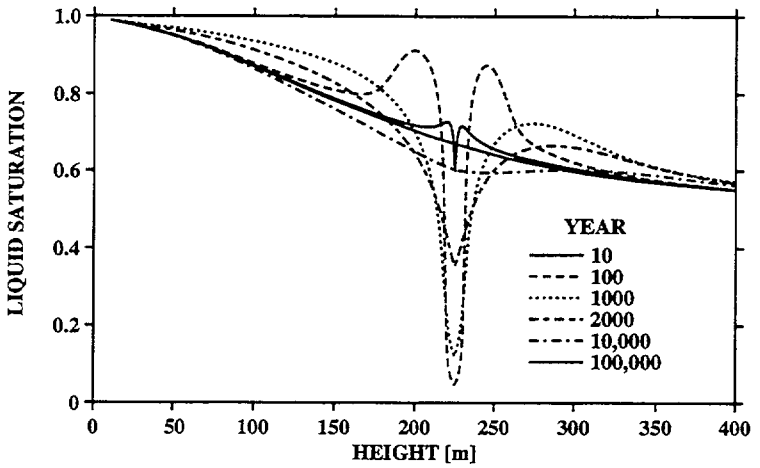

Figure 3-29. Liquid saturation profiles for the indicated times for the low-permeability case

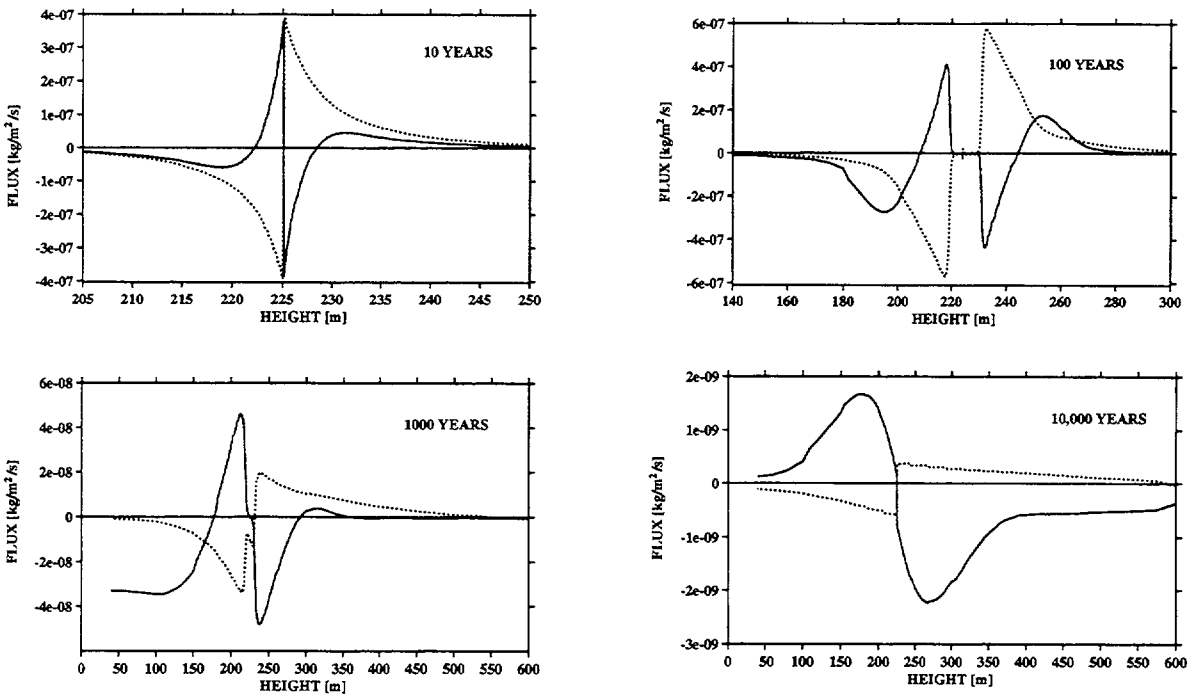

Figure 3-30. Liquid (solid curve) and vapor (dotted curve) flux profiles at the indicated times for the low-permeability case

Table 3-3. Stratigraphic units used in the multilayer model giving the depth from the surface and material properties. A common fracture permeability of log k = -11 and fracture porosity of 0.0018 was used for all layers.

Stratigraphic Unit	Tiva Canyon	Paintbrush	Topopah Spring	Calico Hills
Depth (m)	0 to 100	100 to 150	150 to 475	475 to 600
Matrix permeability [millidarcies]	0.0019	18.0	0.0019	18.0
Matrix porosity	0.1	0.4	0.1	0.4
Equivalent continuum permeability [millidarcies]	18.0	35.97	18.0	35.97
Residual saturation	0.08	0.04	0.08	0.085
α (matrix) x 10^7	5.8	3.12	5.8	4.496
β (matrix)	1.798	1.22	1.798	1.496
Rock density [kg m^{-3}]	2,480	2,300	2,480	2,300
cdry [W/m C]	1.9	1.02	1.9	1.02
cwet [W/m C]	2.34	1.35	2.34	1.35

3.2.1 Stratigraphic Sequence

The values for material properties defining the stratigraphic sequence used in the multilayer model calculations are given in Table 3-3. Fracture properties are the same as used in the base case above. A schematic diagram of the repository location and stratigraphic sequence used in the calculations is shown in Figure 3-31 giving the thickness of each layer and the location of the repository. The abbreviations used in the figure refer to the welded Tiva Canyon tuff (TCw), nonwelded Paint Brush tuff (PTn), welded Topopah Spring unit (TSw), and the vitrified, nonwelded Calico Hills unit (CHnv).

3.2.2 Results

The temperature, liquid saturation and relative humidity, and flux are compared with the results of Pruess and Tsang (1994), who based their calculations on the use of enhanced vapor diffusion. In Figure 3-32, the temperature profile is shown at different times indicated in the figure with and without enhanced vapor diffusion for the 57-kW/acre APD case, and in Figure 3-33 for the 114-kW/acre case. The temperature profiles are approximately the same with or without enhanced vapor diffusion. The peak temperatures are somewhat less with enhanced vapor diffusion, a consequence of more rapid cooling of the repository. The formation of a heat-pipe is clearly visible in the 100-yr temperature profile at 114-kW/acre APD for the case without enhanced vapor diffusion.

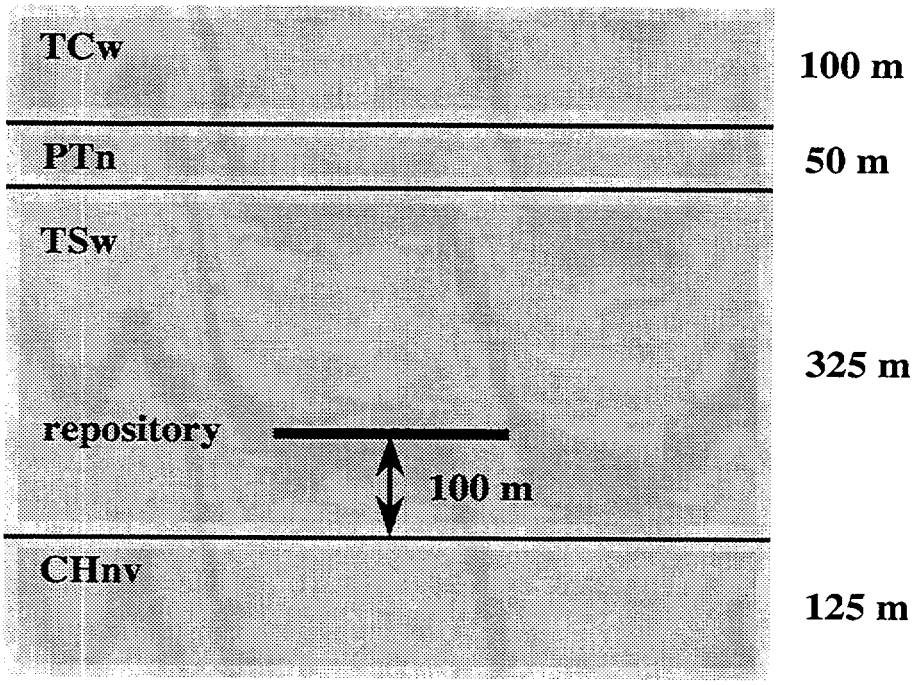

Figure 3-31. Schematic diagram of the multilayer repository model

The corresponding liquid saturation and relative humidity profiles are shown in Figure 3-34 for the 57-kW/acre loading and in Figure 3-35 for 114-kW/acre loading, for the same times as in the previous figure. The saturation and relative humidity profiles indicate a significant difference between enhanced vapor diffusion and the base case for the lower heat load. Much greater dryout occurs with enhanced diffusion compared to without. In Figure 3-35 it should be noted that the relative humidity was not computed in the region of complete dryout for the 100-yr case.

The liquid and vapor fluxes are shown in Figure 3-36 for the 57-kW/acre case for an elapsed time of 100 yr. The solid curves refer to liquid and the dotted curves to vapor. The liquid flux is approximately equal in magnitude with or without enhanced vapor diffusion while the gas flux indicates significant differences. An upward vapor flux is present across the repository horizon in the case of enhanced vapor diffusion. The liquid and vapor fluxes are shown in Figure 3-37 for the 114-kW/acre case for an elapsed time of 100 yr. From the flux profiles, it is clear that a heat-pipe occurs both with and without enhanced vapor diffusion to the extent that counterflow of liquid and vapor occurs both above and

below the repository. However, the heat-pipe is much more pronounced above the repository for both cases. For the case without enhanced vapor diffusion, the vapor flux is downward across the repository horizon. The liquid flux is approximately equal in magnitude with or without enhanced vapor diffusion, while the gas flux indicates significant differences as would be expected.

The results with enhanced vapor diffusion should be comparable to the results presented by Pruess and Tsang (1994). However, significant differences appear to exist between the two calculations, in spite of the fact that the codes used (CTOUGH and TOUGH2) are, or should be, very similar since both are a derivative of the same original TOUGH code (Pruess, 1987). Pruess and Tsang (1994) obtain a greater liquid saturation at the repository horizon compared to this study. This could be due to the extremely coarse grid they have used in their calculations. Without enhanced vapor diffusion, the liquid saturation obtained in this study is much larger than the Pruess and Tsang (1944) result. The discrepancy is more pronounced at lower heat loadings of the repository. Pruess and Tsang (1994) never mention the formation of a heat-pipe for the 114-kW/acre heat load, possibly because transport appears to be diffusion rather than advective dominated.

There exists a much greater difference between enhanced vapor diffusion and the base case at the low-heat load compared to the high-heat load. As is apparent from the figures, the liquid saturation can give a misleading estimate of how wet the dryout region really is. The relative humidity appears to be a much better indicator of the wetness condition of the repository.

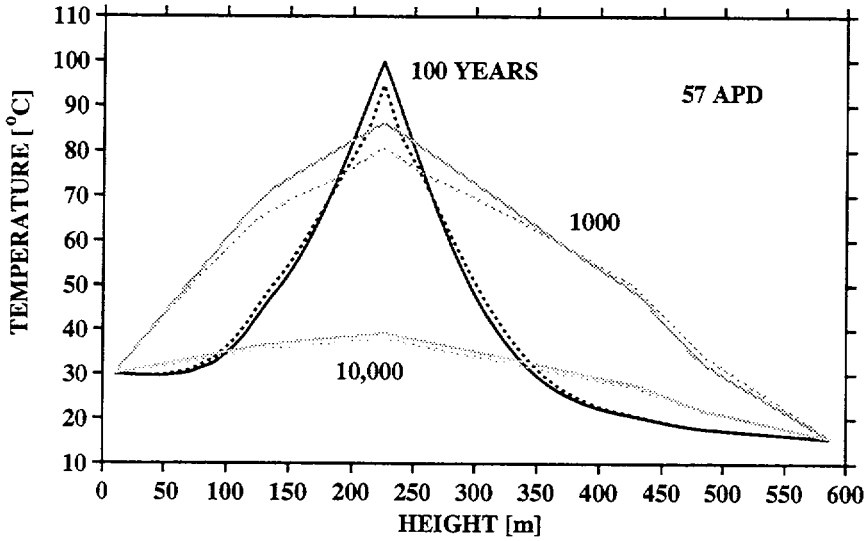

Figure 3-32. Temperature profiles for the 57-kW/acre loading plotted at the indicated times with (dotted curves) and without (solid curves) enhanced vapor diffusion

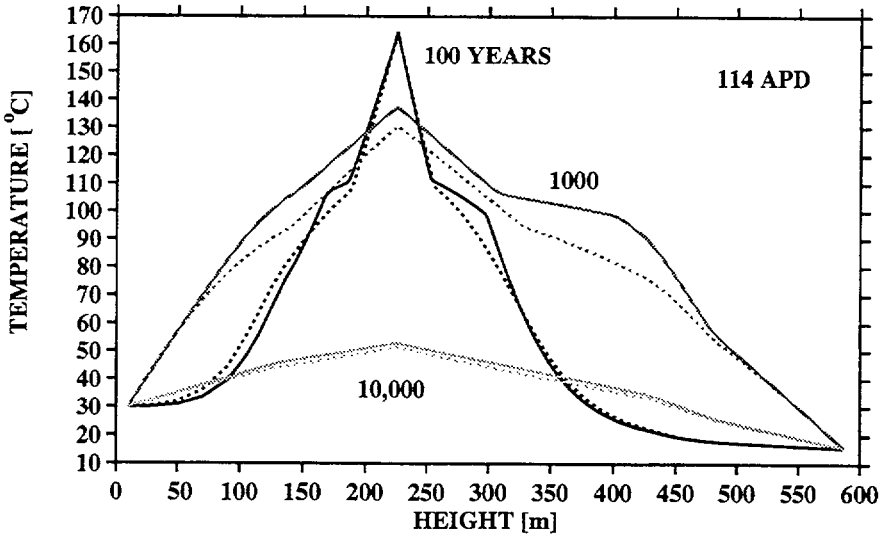

Figure 3-33. Temperature profiles for the 114-kW/acre loading at the indicated times with (solid curves) and without (dotted curves) enhanced vapor diffusion

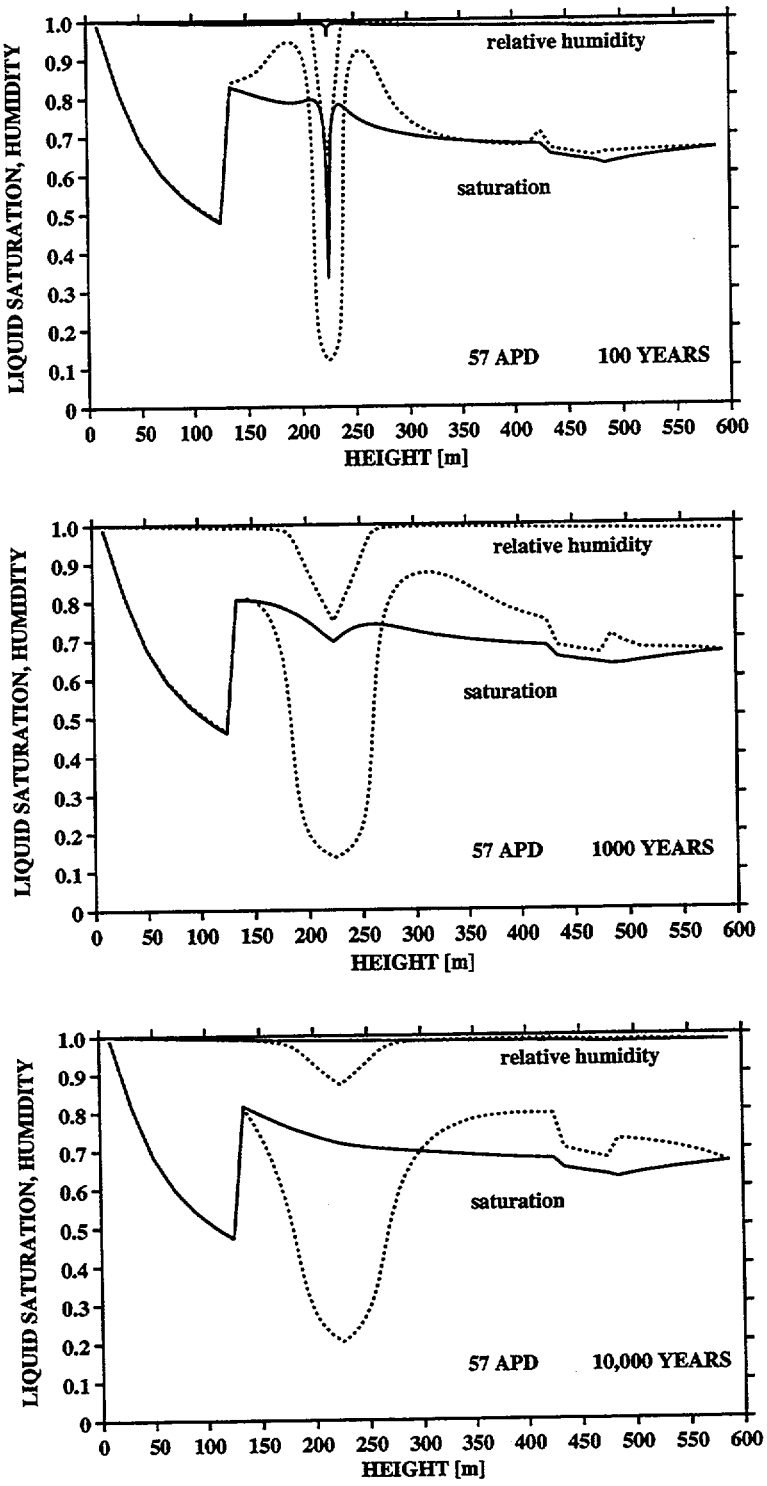

Figure 3-34. Liquid saturation and relative humidity profiles for 57-kW/ acre loading at the indicated times comparing enhanced vapor diffusion (dotted curve) with the base case (solid curve)

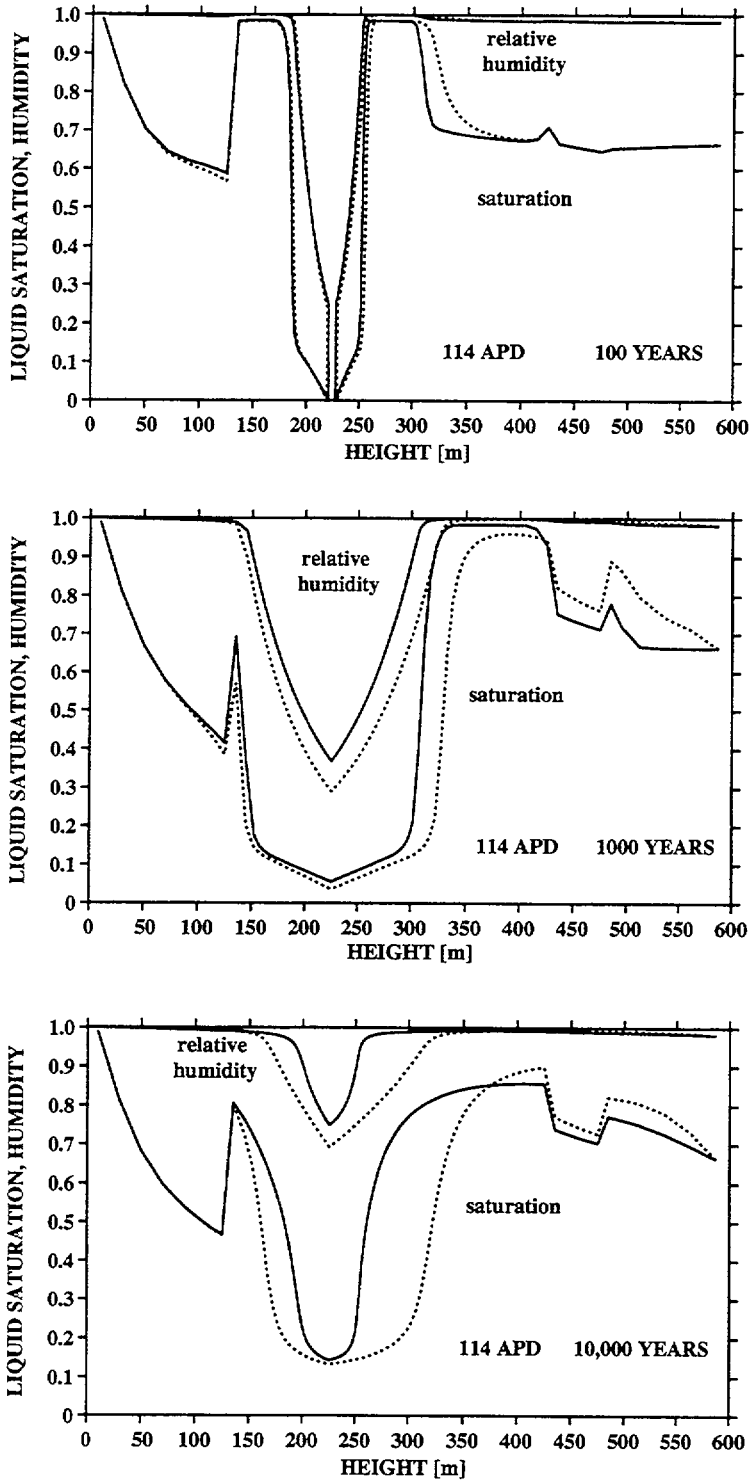

Figure 3-35. Liquid saturation and relative humidity profiles for 114-kW/ acre loading at the indicated times comparing enhanced vapor diffusion (dotted curve) with the base case (solid curve)

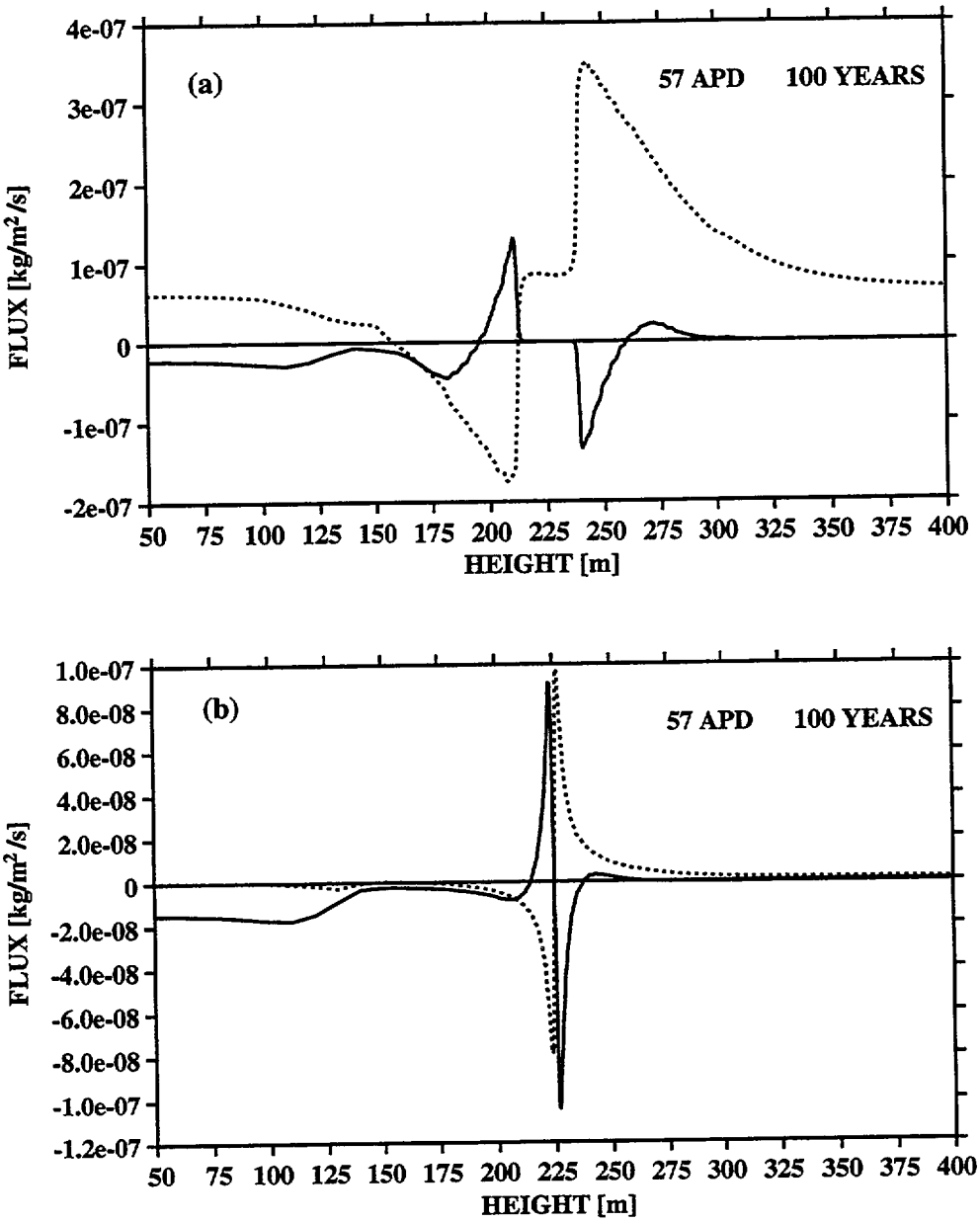

Figure 3-36. Gas and liquid flux profiles for 57-kW/acre loading after 100 yr comparing (a) enhanced vapor diffusion, with (b) the base case. Solid lines refer to liquid and dotted to vapor.

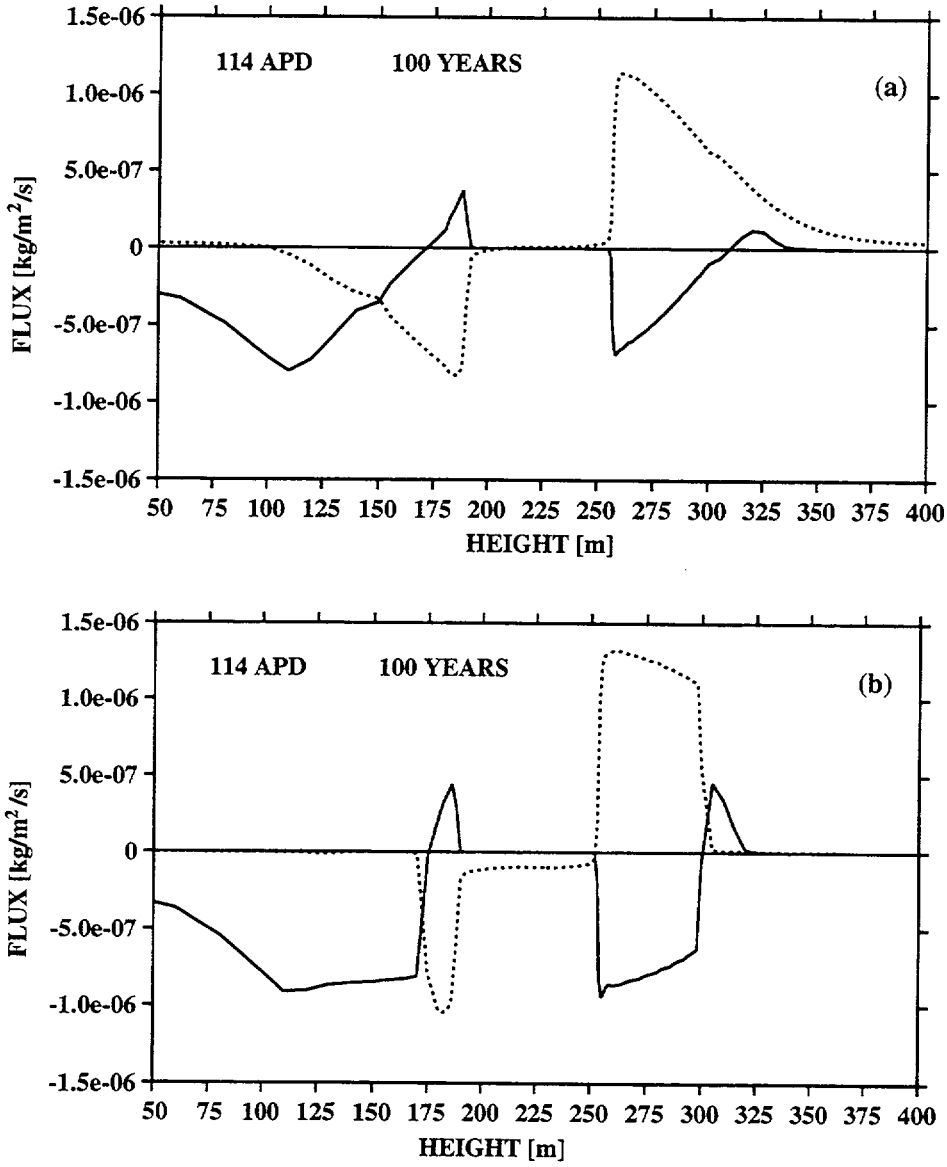

Figure 3-37. Gas and liquid flux profiles for 114-kW/acre loading after 100 yr comparing (a) enhanced vapor diffusion, with (b) the base case. Solid lines refer to liquid and dotted to vapor.

4 SUMMARY AND RECOMMENDATIONS

Calculations were carried out using the two-phase fluid flow code CTOUGH, a modified version of VTOUGH (Nitao, 1988) to simulate the redistribution of moisture in the near-field environment of a HLW repository. A repository-scale model was used in which the repository was represented as a disk and cylindrical symmetry was imposed on the system. Calculations were based on the equivalent continuum model in which the fracture network and matrix are represented by a single homogeneous porous medium. Both single- and multiple-layer media were considered in the simulations. It was found that the results of CTOUGH calculations based on 1D simulations were comparable with 2D results near the center of the repository. The effects of different repository loadings, vapor pressure lowering, and enhanced vapor diffusion on repository dryout were investigated, as well as formation of heat-pipes in the high-thermal loading case. The formulation of enhanced vapor diffusion, given by Pruess and Tsang (1993, 1994) extrapolated from soil data, was investigated. It was found that their formulation of vapor diffusion could grossly overestimate vapor diffusion in tuffaceous rock, especially at low heat loads.

It was noted that the equivalent continuum model may not be adequate to describe infiltration in fractured tuff because of the assumption of capillary equilibrium between matrix and fractures. This concern may also apply to movement of water from the perched reservoir above the repository created by condensation of vapor and, hence, could represent a significant limitation of the equivalent continuum model in predicting moisture contact with waste packages.

Incorporating the equivalent continuum model formulation in performance assessment-type models should be feasible from a computational point of view for 1D geometry. However, it is highly questionable, from a physical point of view, how meaningful the results really are and to what extent the equivalent continuum model is able to capture the actual behavior of the repository environment. In this regard it is noted that vapor transport is predicted by the model in certain circumstances to be downward, rather than upward, at the repository horizon. This could have significant implications in a description of CO_2 transport, for example.

Relative humidity was found to provide a more sensitive indicator of the moisture content of the repository compared to liquid saturation. Humidity may be an important factor in consideration of the near-field region, because corrosion of steel can take place under humid conditions even if liquid water is not present.

Several recommendations for future work are listed below:

- There is a need to resolve the discrepancy between the results obtained in the present work and that of Pruess and Tsang (1994). The results obtained in this study for the multilayer model do not agree with the results presented by Pruess and Tsang (1994), although, with one exception, presumably identical values for material properties were used in both calculations. The one exception known to the authors is the use of a common fracture permeability in all units including the nonwelded Paint Brush and Calico Hills stratigraphic units. Pruess and Tsang (1994) assumed matrix-only properties for these units. However, because of the comparatively large matrix permeability in these units, this is not expected to significantly change the results.

- Model calculations should be extended to include the multiple interacting continua model which provides for disequilibrium between fractures and the rock matrix. The equivalent continuum model is very likely inadequate for describing the interaction between fracture and

matrix transport and may grossly underestimate moisture content near the waste packages. A multiple interacting continuum model should be developed which allows the requirement of capillary equilibrium between fracture and matrix, the cornerstone, and possibly, Achilles heel of the equivalent continuum model, to be relaxed. However, a possible concern with implementation of this model might be obtaining sufficient data for the various parameters which enter the model describing communication between the matrix blocks and the fracture network. Experiments may need to be devised to obtain such data.

- Vapor transport in tuffaceous rock such as characterizes YM must be better understood, especially with regard to the phenomenon of enhanced vapor transport observed in soils. To this end, basic experimental work should be conducted on diffusion of vapor and noncondensable gases in partially saturated tuff rock at elevated temperatures. The experimental work should span a wide range of temperatures, saturations, and values of relative humidity. Diffusion rates with and without the presence of fractures should be considered. In addition the question of whether water vapor diffusion is accelerated in the Knudsen region should be addressed. Important factors considered should be the role of tortuosity and porosity, which are absent from the formulation given by Pruess and Tsang (1994). The fact that the tuff matrix may have a tortuosity as low as 0.01 or less could counter the enhancement effects observed in soils.

- Because capillary forces play a dominant role in the redistribution of moisture, they must be better understood, especially regarding fracture properties. The temperature behavior of the van Genuchten parameters for material properties is presently completely unknown and needs to be understood.

- The importance of various uncertain parameters, such as the vapor diffusion rate, tortuosity, unsaturated fracture-liquid permeability, and others on repository and waste package dryout requires additional examination. Simulations could be conducted to determine when and how each parameter is important to performance. For example, the van Genuchten parameters currently used to describe partially saturated liquid flow in fractures are likely to be extremely important in phenomena such as heat-pipe formation. However the numbers currently used may have little or no technical basis and their temperature dependence is unknown.

5 REFERENCES

Ali, M.S., F.G. King, and S. Ilias. 1994. Diffusive transport of carbon dioxide through USW-G4 Topopah Spring Tuffs. *Material Research Society* 333: 827–834.

Benard, R.W., M.L. Wilson, H.A. Dockery, J.H. Gauthier, P.G. Kaplan, R.R. Eaton, F.W. Bingham, and T.H. Robey. 1992. *TSPA 1991: An Initial Total-System Performance Assessment for Yucca Mountain.* SAND91-2795. Albuquerque, NM: Sandia National Laboratories.

Bird, R.B., W.E. Stewart, and E.N. Lightfoot. 1960. *Transport Phenomena.* New York, NY: John Wiley and Sons.

Buscheck, T.A., and J.J. Nitao. 1992. The impact of thermal loading on repository performance at Yucca Mountain. *Proceedings of the Third Annual High-Level Radioactive Waste Management Conference.* La Grange Park, IL: American Nuclear Society. 1,003–1,017.

Codell, R., N. Eisenberg, D. Fehringer, W. Ford, T. Margulies, T. McCartin, J. Park, and R. Randall. 1992. *Initial Demonstration of the NRC's Capability to Conduct a Performance Assessment for a High-Level Waste Repository.* NUREG-1327. Washington, DC: Nuclear Regulatory Commission.

Green, R.T., R.D. Manteufel, F.T. Dodge, and S.J. Svedeman. 1992. *Theoretical and Experimental Investigation of Thermohydrologic Processes in a Partially Saturated, Fractured Porous Medium.* NUREG/CR-6026. Washington, DC: Nuclear Regulartory Commission.

Jury, W.A., and J. Letey, Jr. 1979. Water vapor movement in soil: Reconciliation of theory and experiment. *Soil Science Society of America Journal* 43: 823–827.

Lichtner, P.C. 1994. *Multi-Phase Reactive Transport Theory.* CNWRA 94-018. San Antonio, TX: Center for Nuclear Waste Regulatory Analyses.

Nitao, J.J. 1989. *V-TOUGH–An Enhanced Version of the TOUGH Code for the Thermal and Hydrologic Simulation of Large-Scale Problems in Nuclear Waste Isolation.* UCID-21954. Livermore, CA: Lawrence Livermore National Laboratory.

Nitao, J.J. 1988. *Numerical Modeling of the Thermal and Hydrological Environment Around a Nuclear Waste Package Using the Equivalent Continuum Approximation: Horizontal Emplacement.* UCID-21444. Livermore, CA: Lawrence Livermore National Laboratory.

Nuclear Regulatory Commission. 1994. Disposal of high-level radioactive wastes in geologic reporitories. *Code of Federal Regulations, Title 10, Energy, Part 60 (10 CFR Part 60).* Washington, DC: Office of the Federal Register: National Archives and Records Administration: 91–124.

Peters, R.R., and E.A. Klavetter. 1988. A continuum model for water movement in an unsaturated fractured rock mass. *Water Resources Research* 24: 416–430.

Pruess, K., J.S.Y. Wang, and Y. W. Tsang. 1990a. On thermohydrologic conditions near high-level nuclear wastes emplaced in partially saturated fractured tuff. 1. Simulation studies with explicit consideration of fracture effects. *Water Resources Research* 26: 1,235–1,248.

Pruess, K., J.S.Y. Wang, and Y. W. Tsang. 1990b. On thermohydrologic conditions near high-level nuclear wastes emplaced in partially saturated fractured tuff. 2. Effective continuum approximation. *Water Resources Research* 26: 1,249–1,261.

Pruess, K. 1987. *TOUGH User's Guide*. NUREG/CR-4645. Washington, DC: Nuclear Regulatory Commission.

Pruess, K. 1991. *TOUGH2—A General-Purpose Numerical Simulator for Multiphase fluid and Heat Flow.* LBL-29400. Berkeley, CA: University of California: Lawrence Berkeley Laboratory.

Pruess, K., and Y. Tsang. 1993. Modeling of strongly heat-driven flow processes at a potential high-level nuclear waste repository at Yucca Mountain, Nevada. *Proceedings of the Fourth High-Level Radioactive Waste Management Conference*. La Grange Park, IL: American Nuclear Society. 568–575.

Pruess, K., and Y. Tsang. 1994. *Thermal Modeling for a Potential High-Level Nuclear Waste Repository at Yucca Mountain, Nevada.* LBL-35381, UC-600. Berkeley, CA: Lawrence Berkeley Laboratory.

Ross, B. 1984. A conceptual model of deep unsaturated zones with negligible recharge. *Water Resources Research* 20: 1,627–1,629.

Tsang, Y.W., and K. Pruess. 1987. A study of thermally induced convection near a high-level nuclear waste repository in partially saturated fractured tuff. *Water Resources Research* 23: 1,958–1,966.

van Genuchten, M. 1980. A closed form equation for predicting the hydraulic conductivity of unsaturatedsoils. *Soil Science Society of America Journal* 44: 892–898.

Vargaftik, N.B. 1975. *Tables on the Thermophysial Properties of Liquids and Gases.* Second Edition. New York, NY: John Wiley and Sons.

Walker, W.R., J.D. Sabey, and D.R. Hampton. 1981. *Studies of Heat Transfer and Water Migration in Soils*. Final Report. Fort Colins, CO: Colorado State University: Department of Agricultural and Chemical Engineering,

Wescott, R.G., M.P. Lee, N.A. Eisenberg, and T.J. McCartin. 1994. *Initial Demonstration of the NRC's Capability to Conduct a Performance Assessment for a High-Level Waste Repository.* NUREG-1464. Washington, DC: Nuclear Regulatory Commission.

Wilson, M.L., J.H. Gauthier, R.W. Barnard, G.E. Barr, H.A. Dockery, E. Dunn, R.R. Eaton, D.C. Guerin, N. Lu, M.J. Martinez, R. Nilson, C. A. Ratuman, T.H. Robey, B. Ross, E.E. Ryder, A.D. Lamont, I.R. Triay, A. Meijer, and D.E. Morris. 1994. *Total-System Performance Assessment for Yucca Mountain—SNL Second Iteration (TSPA-1993).* SAND93-2675, UC-814. Albuquerque, NM: Sandia National Laboratories.

Wolfram, S. 1991. *Mathematica, a System for Doing Mathematics by Computer.* Second Edition, New York, NY: Addison-Wesley.

Zyvoloski, G., Z. Dash, and S. Kelkar. 1992. *FEHMN 1.0: Finite Element Heat and Mass Transfer Code.* LA-12062-MS, Rev 1. Los Alamos, NM: Los Alamos National Laboratory.